Monthly Notices
of the
ROYAL ASTRONOMICAL SOCIETY

MNRAS **530,** 318–339 (2024) https://doi.org/10.1093/mnras/stae508
Advance Access publication 2024 February 21

NGTS-28Ab: a short period transiting brown dwarf

Beth A. Henderson ,[1★] Sarah L. Casewell,[1★] Michael R. Goad,[1] Jack S. Acton ,[1] Maximilian N. Günther ,[2] Louise D. Nielsen,[3] Matthew R. Burleigh,[1] Claudia Belardi,[1] Rosanna H. Tilbrook,[1] Oliver Turner ,[4] Steve B. Howell,[5] Catherine A. Clark,[6,7] Colin Littlefield,[5,8] Khalid Barkaoui ,[9,10,11] Douglas R. Alves ,[12,13] David R. Anderson ,[14,15] Daniel Bayliss ,[14,15] Francois Bouchy,[4] Edward M. Bryant ,[16] George Dransfield,[17] Elsa Ducrot,[18†] Philipp Eigmüller,[19] Samuel Gill,[14,15] Edward Gillen ,[20,21] Michaël Gillon ,[9] Faith Hawthorn ,[14,15] Matthew J. Hooton ,[22] James A. G. Jackman ,[14,15,23] Emmanuel Jehin,[24] James S. Jenkins,[13,25] Alicia Kendall,[1] Monika Lendl ,[4] James McCormac,[14,15] Maximiliano Moyano,[26] Peter Pihlmann Pedersen,[22,27] Francisco J. Pozuelos,[28] Gavin Ramsay ,[29] Ramotholo R. Sefako,[30] Mathilde Timmermans,[9] Amaury H. M. J. Triaud ,[17] Stephane Udry,[4] Jose I. Vines,[26] Christopher A. Watson,[31] Richard G. West ,[14,15] Peter J. Wheatley [14,15] and Sebastián Zúñiga-Fernández [9]

Affiliations are listed at the end of the paper

Accepted 2024 February 13. Received 2024 January 31; in original form 2023 January 3

ABSTRACT

We report the discovery of a brown dwarf orbiting a M1 host star. We first identified the brown dwarf within the Next Generation Transit Survey data, with supporting observations found in *TESS* sectors 11 and 38. We confirmed the discovery with follow-up photometry from the South African Astronomical Observatory, SPECULOOS-S, and TRAPPIST-S, and radial velocity measurements from HARPS, which allowed us to characterize the system. We find an orbital period of ∼1.25 d, a mass of $69.0^{+5.3}_{-4.8}$ M_J, close to the hydrogen burning limit, and a radius of $0.95 \pm 0.05\,R_J$. We determine the age to be >0.5 Gyr, using model isochrones, which is found to be in agreement with spectral energy distribution fitting within errors. NGTS-28Ab is one of the shortest period systems found within the brown dwarf desert, as well as one of the highest mass brown dwarfs that transits an M dwarf. This makes NGTS-28Ab another important discovery within this scarcely populated region.

Key words: (stars:) brown dwarfs.

1 INTRODUCTION

Brown dwarfs (BDs) are intriguing objects, located between high-mass exoplanets and low-mass main-sequence stars. Their masses are canonically defined to lie in the 13–80 M_J range (Burrows & Liebert 1993; Baraffe et al. 2002; Burgasser 2008; Triaud et al. 2017). BDs never become massive enough to burn hydrogen in their core, supporting themselves through electron degeneracy pressure (Whitworth 2018), although some BDs are massive enough to burn deuterium (Bate, Bonnell & Bromm 2002; Whitworth 2018). The first BDs were not discovered until 1995 (Gliese 229B: Nakajima et al. 1995; Teide 1: Rebolo, Zapatero Osorio & Martín 1995) but candidates were found with radial velocity methods previous to this (HD114762: Latham et al. 1989). However, thousands have since been observed with the majority being isolated BDs.

Due to their degenerate nature, BDs exhibit an age–radius–mass–temperature degeneracy: their radii contract over their lifetimes as they cool (Burrows & Liebert 1993). If the radius can be determined, how the BD evolves over their lifetimes can be predicted and therefore can be used as an age estimate (e.g. Baraffe et al. 2003, 2015; Marley et al. 2021). However, most BDs do not have accurately measured radii due to being isolated objects. BDs found in eclipsing binary systems therefore offer an opportunity to directly measure their radii, breaking this degeneracy.

Only two BD–BD eclipsing binary systems are known to date (Stassun, Mathieu & Valenti 2006; Triaud et al. 2020), and searching for BDs around main-sequence stars is an obvious place to look. Fortunately, BD radii are similar to that of Jupiter (Burrows & Liebert 1993) making them as detectable as Jupiter-sized exoplanets in exoplanet surveys (e.g. Acton et al. 2021; Carmichael et al. 2021; Grieves et al. 2021).

However, the radii of BDs can also be affected by exterior factors to the BD, such as interactions with their host star through irradiation (Casewell et al. 2020b). Irradiation will affect the BD atmosphere by heating it, and is also thought to cause a BD's radius to be inflated

★ E-mail: bah26@leicester.ac.uk (BAH); slc25@leicester.ac.uk (SLC)
† Paris Region Fellow, Marie Sklodowska-Curie Action

(e.g. Kelt-1b: Siverd et al. 2012; WD1032+11: Casewell et al. 2020a) in the same way that is seen for hot Jupiters (e.g. Thorngren et al. 2021; Tilbrook et al. 2021; Alves et al. 2022).

To date, 34 transiting BDs have been discovered orbiting within 3 au of a main-sequence star (e.g. Carmichael et al. 2022 and references therein) which is small compared to the thousands of isolated BDs. This number is also much lower than would be expected when compared to the population of low-mass eclipsing binary systems or the hot Jupiter exoplanet population. This local minima between these populations is called the 'BD desert' (Grether & Lineweaver 2006). The desert is thought to be caused by the differences in formation mechanisms between exoplanets and stars (Ma & Ge 2014; Grieves et al. 2021) but is still not well understood.

Since it was first identified, the BD desert is still scarcely populated, even including recent works using large photometric surveys (see fig. 7 of Triaud et al. 2017). Multiple studies have looked into characteristics of objects within the BD desert. Ma & Ge (2014) discussed whether there is a relationship between mass of the BD and eccentricity. They considered all-known exoplanets (at the time), along with all BD candidates around FGK stars (spanning 0–100 M_J) and determined that they could separate BDs at a mass of 42.5 M_J into two populations. Those which are more massive (>42.5 M_J) appeared to display a period-eccentricity distribution with a circularization limit of ∼12 d, similar to stellar binaries. This is due to objects with shorter periods (up to 12 d) having circular orbits, and those with longer orbits having a flat but wide distribution of eccentricities (as seen in Raghavan et al. 2010; Ma & Ge 2014). The lower mass population displayed a period–eccentricity trend similar to exoplanets, where higher mass objects (up to the 42.5 M_J split) have lower eccentricities. Ma & Ge (2014) determined that these trends point to objects with masses above 42.5 M_J forming via stellar formation mechanisms, instead of via protoplanetary discs (Ma & Ge 2014).

Other studies have since sought to find this split population in eccentricity distributions within their observed sample of BDs. Grieves et al. (2021) state that they do not see this trend or evidence of Ma & Ge (2014)'s split population at 42.5 M_J. Although they note their small sample size, as they only include transiting BDs and low-mass stars (12.9 M_J to 149.8 M_J, Grieves et al. 2021) and not high mass exoplanets. Carmichael, Latham & Vanderburg (2019) also does not find a split at 42.5 M_J. However, they conclude it is due to there not being a split in the population at all, as opposed to a lack of objects. This illustrates a clear need for more objects to populate this region, to aid in the understanding of whether there is a mass split at 42.5 M_J due to formation mechanisms.

Metallicity ([Fe/H]) has also been looked at within the BD sample. Ma & Ge (2014) did not find any evidence of a split population at 42.5 M_J when comparing [Fe/H], and found a mean [Fe/H] of −0.05. Jenkins et al. (2015) compared the mean [Fe/H] values for BDs, stellar binaries, and exoplanets. They found that BDs and stellar binaries have comparable subsolar mean [Fe/H] values, whereas exoplanets have an above solar mean [Fe/H]. The BDs within the Jenkins et al. (2015) sample were mainly found with radial velocity methods, rather than the transiting sample as is done in this work.

In this paper, we present the discovery of NGTS-28Ab, a transiting BD lying within the 'BD desert'. In Section 2, we detail the various photometric and spectral observations obtained. In Section 3, the methods used to analyse both the host star and BD are described, along with the probable common proper motion companion, NGTS-28B. Section 4 discusses the importance of this discovery in terms of its position within the BD desert and analyses the eccentricity and age of NGTS-28Ab further.

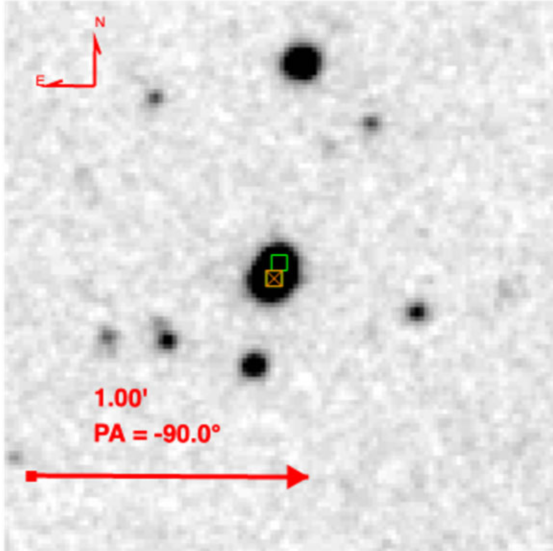

Figure 1. DSS image showing NGTS-28A (orange box with cross) and NGTS-28B (green box) blended on sky, along with other nearby objects. North and east are shown on the figure in the top left corner as well as a 1 arcmin position angle (PA) arrow for scale.

2 OBSERVATIONS

There is a star located ∼4 arcsec from NGTS-28A, meaning the photometry of NGTS-28A was blended with that nearby object, hereafter referred to as NGTS-28B. NGTS-28B is of similar magnitude and is likely a common proper motion companion to NGTS-28A (see Section 3.1). NGTS-28AB refers to the combination of both NGTS-28A and NGTS-28B, where both stars are present in a photometric aperture. NGTS-28AB was first observed with the Next Generation Transit Survey (NGTS; Wheatley et al. 2018) and later the *Transiting Exoplanet Survey Satellite* (*TESS*; Ricker et al. 2014). Due to NGTS and *TESS* having pixel sizes of 5 arcsec (Wheatley et al. 2018) and 21 arcsec (Ricker et al. 2014), respectively, the photometry from both these facilities of NGTS-28A was blended with that of NGTS-28B (Fig. 1). We obtained follow-up observations in various wavelengths (Table 1) using SHOC on the 1 m Lesedi telescope at the South African Astronomical Observatory (SAAO; Coppejans et al. 2013) to obtain observations that were not blended. We obtained follow up photometry with SPECULOOS-S and TRAPPIST-S, most of which were uncontaminated by NGTS-28B. We obtained six spectra in total with HARPS (Mayor et al. 2003), four of the host star NGTS-28A, and two of NGTS-28B. A summary of these observations can be found in Tables 1 and 2.

2.1 Photometry

2.1.1 NGTS

NGTS-28A was initially observed with NGTS a twelve-telescope array situated at ESO's Paranal Observatory, Chile (Wheatley et al. 2018). The observations taken between the dates 2017 January 2 to 2017 August 21. The twelve, 20 cm telescopes cover almost 100 deg^2 of sky and operate in a custom bandpass of 520–890 nm (Wheatley

Table 1. Photometric observations of *NGTS-28Ab*.

Instrument	Bandpass	Cadence (s)	Number of transits	Observation date
NGTS	520–890 nm	13	26	2017 Jan 2 to 2017 Aug 21
TESS Sector 38	600–1000 nm	120	20	2021 Apr 29 to 2021 May 25
TESS Sector 11	600–1000 nm	1800	16	2019 Apr 22 to 2019 May 21
SAAO	I	10 s	1	2018 July 4
SPECULOOS-S	g', r', i'	147, 52, 26	3	2023 Apr 18
SPECULOOS-S	z', $I+z'$	19, 12	2	2023 June 15
TRAPPIST-S	z'	60	1	2023 Mar 29
TRAPPIST-S	$I+z'$	45	1	2023 Apr 18

Table 2. Radial velocity measurements of *NGTS-28A* and *NGTS-28B* and the associated uncertainties and BIS values from HARPS.

BJD	Radial velocity (km s^{-1})	BIS (km s^{-1})
	NGTS-28A	
2459405.599495	-13.99 ± 0.049	-0.34 ± 0.10
2459409.590870	-20.22 ± 0.055	1.08 ± 0.11
2459410.492873	-4.38 ± 0.053	2.87 ± 0.11
2459412.475762	9.46 ± 0.049	0.37 ± 0.10
	NGTS-28B	
2459376.625674	-2.01 ± 0.048	0.06 ± 0.10
2459377.543570	-1.75 ± 0.049	0.76 ± 0.10

et al. 2018). We observed for a total of 135 nights, during which we obtained 199 319 science images with a 13 s cadence.

The raw images were processed following the method discussed in Wheatley et al. (2018) and the light curves were detrended using SYSREM (Tamuz, Mazeh & Zucker 2005). After detrending, transits were detected using a BOXED LEAST SQUARES algorithm. A total of 26 transits were detected, which can be seen in Fig. 2 and a phase-fold of the data on the predicted period can be seen in Fig. 3. The star is clearly variable, but we determined an orbital period of 1.25 d and a transit depth of around 1.36 per cent.

2.1.2 TESS

TESS obtained 30 min cadence photometry of NGTS-28AB, observing between 2019 April 22 to 2019 May 21 for sector 11 and 2021 April 29 to 2021 May 25 for sector 38. Sector 38 also had 2-min cadence data. The 30 min full frame image has a precision around 5 mmag (Ricker et al. 2014). Fig. 4 shows the full SPOC light curve, along with a cropped version showing a flare and the individual transits.

The transits within both *TESS* sectors were independently identified by the *TESS* team and NGTS-28B was initially named TOI (*TESS* Object of Interest) 4339 on 2022 September 09. NGTS-28A has since been found to be the true host star. NGTS-28A was named TOI 6110 on 2023 May 27. The 2-min cadence data was processed using the SPOC pipeline (Jenkins et al. 2016). As with the NGTS data, the *TESS* photometry is blended. *TESS* provides two flux values: SAP flux and PDCSAP flux. The PDCSAP flux removes systematics in the light curve, as well as correcting for dilution. Within the PDCSAP flux, we noticed the transit depths were much larger than expected. PDCSAP flux light curve has been corrected for dilution, assuming the transit is on the companion star, NGTS-28B and not NGTS-28A. We therefore chose to use SAP flux instead and modelled the data using a Gaussian process (GP) fit during the global modelling process to remove systematics in the data. We also performed our own dilution calculation to use within the global modelling. The *TESS* data contains a total of 20 transits in the 2-min cadence data. Unfortunately, the sector 11 30-min cadence data includes a large (5 d) data gap in the centre of the observation run, despite this it was used to provide confirmation of the ephemeris.

2.1.3 SAAO

We obtained *V*- and *I*-band transit light curves with the SAAO 1.0 m telescope (Table 1) and one of the frame-transfer SHOC (Sutherland High Speed Photometer; Coppejans et al. 2013) CCD cameras, specifically ‘SHOC‘n’awe’, between 2018 and 2020. On the 1.0 m, the SHOC cameras have a pixel scale of 0.167 arcsec pixel^{-1}. Combined with 4 × 4 binning, this gave a pixel resolution of 0.67 arcsec. Both data sets were de-biassed and flat-fielded using SAAO’s local PYTHON-based SHOC reduction pipeline, which utilizes IRAF (Tody 1986, 1993) and PYRAF (Science Software Branch at STScI 2012) tasks.

We used the Starlink package AUTOPHOTOM (Eaton et al. 2014) to perform aperture photometry on both our target and several suitable comparison stars in the 2.85 arcmin × 2.85 arcmin field of view. Since the two stars NGTS-28A and NGTS-28B lie ≈4 arcsec apart, a 2 pixel radius aperture was chosen, together with a background annulus with radius between 12 and 14 pixels, to try to avoid contaminating light. Even so, while the two stars are indeed fully resolved in the SAAO *V*-band images, they are increasingly blended in the longer wavelength *I* filter image.

The measured fluxes of the comparison stars were used to perform differential photometry on each of NGTS-28A and NGTS-28B, which confirms that the transit is on NGTS-28A. While the transit was detected within the SAAO *V* data, we did not use this in our global modelling. This is due to concerns over the noise levels within the data, with a large amount of scatter seen in the baseline.

2.1.4 SPECULOOS-South

We obtained simultaneous, multiwavelength observations of NGTS-28A with the three of the four, 1.0-m ‘Search for Planets EClipsing Ultra-cOOl Stars’ (SPECULOOS-S) telescopes at Cerro, Paranal (Delrez et al. 2018; Jehin et al. 2018; Sebastian et al. 2021). Each SPECULOOS-S telescope is equipped with a 2K × 2K detector with a pixel scale of 0.35 arcsec and an on-sky field of view of 12 × 12 arcmin. On 2023 April 18, we simultaneously observed a transit on NGTS-28A in the Sloan-g', -r' and -i' filters on the Io, Europa and Callisto telescopes, respectively. We also obtained transits in z' and $I + z'$ filters on 2023 June 15 using the Io and Europa telescopes. Details on the cadence for each observation can be found in Table 1.

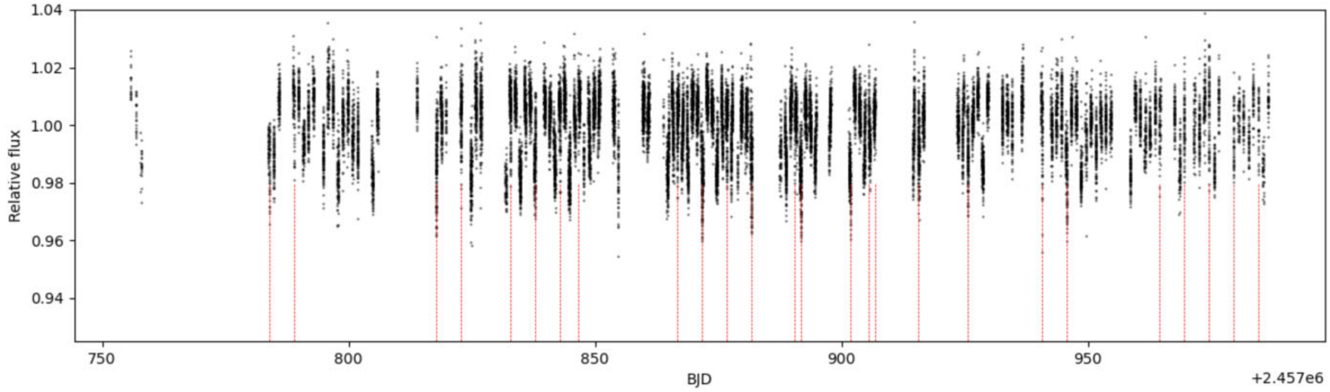

Figure 2. The full NGTS light curve for NGTS-28AB with the transit positions marked by the red dashed lines.

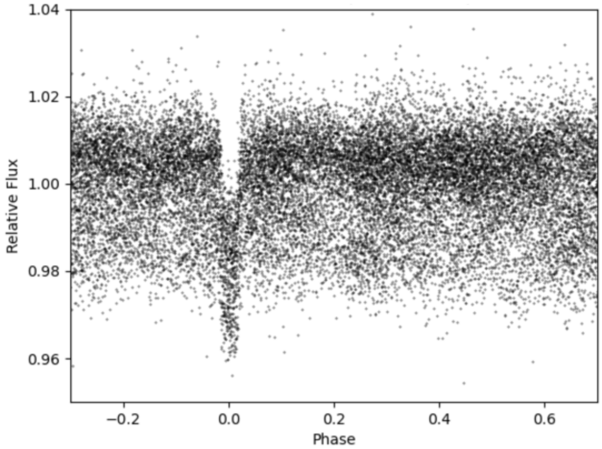

Figure 3. The NGTS light curve, phase-folded on the 1.254145 d period from NGTS.

We processed all of the data following the PROSE pipeline detailed in Garcia et al. (2022). Briefly, PROSE is a modular and adaptable pipeline, which performs image reduction/calibration, then differential aperture photometry on NGTS-28A. The differential aperture photometry creates a weighted, artificial comparison star from all available objects within the image as described in Broeg, Fernández & Neuhäuser (2005). The light curves are then detrended for airmass, full width half-maximum and sky background, with PROSE, producing the normalised, resultant curves seen in Fig. 5. This procedure has been successfully used for previous SPECULOOS-S observations (e.g. Barkaoui et al. 2023; Dransfield et al. 2024).

After performing aperture photometry, we confirmed all the SPECULOOS-S transits, except for the i' filter observation, were uncontaminated. Due to high background in the g' and r' observations, the last few points of each were discarded from global modelling.

2.1.5 *TRAPPIST*

The TRAnsiting Planets and PlanetIsmals Small Telescope (TRAPPIST-S, Gillon et al. 2011; Jehin et al. 2011) is a 0.6 m robotic telescope based at ESO's La Silla Observatory. TRAPPIST-S is equipped with a 2K×2K detector with a 0.6 arcsec pixel scale, and a field of view of 22 × 22 arcmin. Two single-transit observations were taken at TRAPPIST-S. The z' filter observation was made on 2023 March 29, and the $I + z'$ filter observation was made on 2023 April 18. Cadence for each observation can be seen in Table 1. The PROSE pipeline (Garcia et al. 2022) was also used for the TRAPPIST-S data reduction, as in Section 2.1.4. The resultant, relative flux light curves can be seen in Fig. 5.

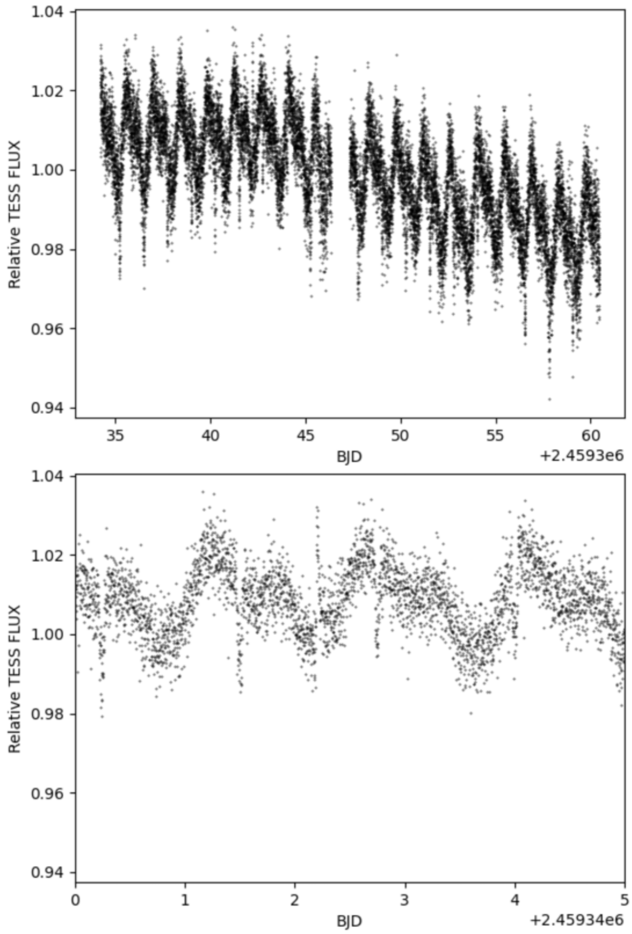

Figure 4. Top: The full *TESS* light curve for NGTS-28AB 2 min cadence data in sector 38, showing the transits. An apparent rotation of the object can also be seen. Bottom: A snippet of the top image, showing the apparent rotation of the object and a flare.

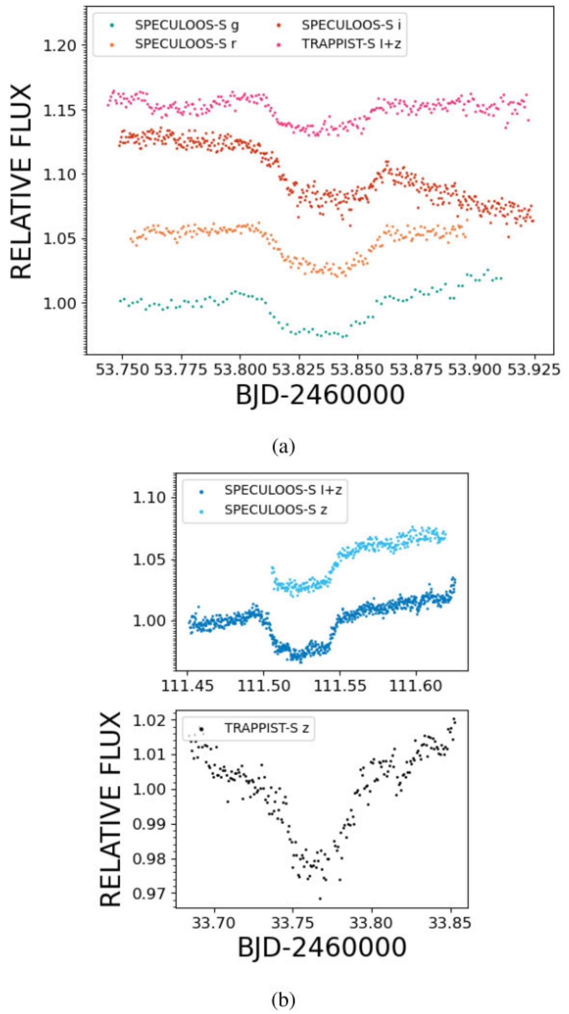

Figure 5. Normalized light curves of the new data from SPECULOOS-S and TRAPPIST-S. Offsets have been applied to some of the fluxes for clarity.

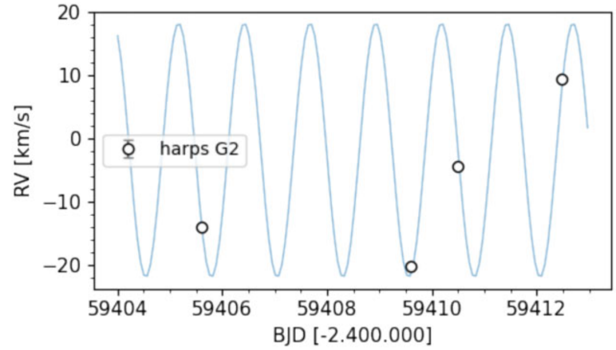

Figure 6. HARPS time series plot of the radial velocity points from the spectra, with a G2 mask used.

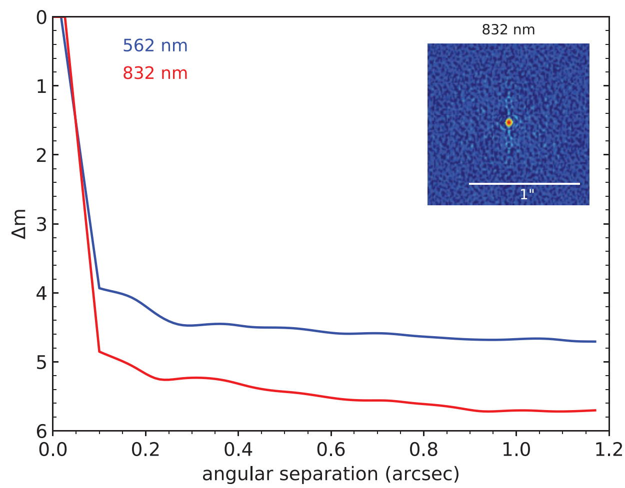

Figure 7. 5σ contrast curves for speckle imaging in both 562 and 832 nm filters. This is plotted as a function of the angular separation from 0.02 to 1.2 arcsec. The reconstructed image for 832 nm can be seen in the top right of the figure. No close companions have been found within these limits.

2.2 Radial velocities

2.2.1 HARPS

We obtained high-resolution spectra of both NGTS-28A and NGTS-28B using HARPS, an echelle spectrograph on ESO's 3.6 m telescope at La Silla Observatory (Mayor et al. 2003). HARPS is fibre-fed with an on-sky diameter of 1 or 1.4 arcsec (Mayor et al. 2003). There is also the option of a second fibre simultaneously monitoring the sky or wavelength solution of the instrument. It covers a spectral range of 380–690 nm, has a resolution of R = 115 000 (Mayor et al. 2003).

For our observations, we used the default high accuracy mode with a 1 arcsec science fibre and fibre B on sky (for more information, see Mayor et al. 2003). We used exposures of 2400 s for each spectrum, except for the final exposure for NGTS-28A which has an exposure time of 1800 s. The spectra had signal-to-noise ratios that ranged between 3.4 and 4.7, and was extracted per pixel in order 50 (corresponding to ∼550 nm). We obtained four spectra of NGTS-28A between 2021 July 10 and 2021 July 16 (Table 2). On 2021 June 11 to 2021 June 12, we also obtained two spectra of NGTS-28B. The mean RV precision reached with the four NGTS-28A observations was 0.0515 km s^{-1}.

The data were reduced using the HARPS pipeline and radial velocities (RVs) measured using a G2V mask and the cross-correlation technique (Baranne et al. 1996; Pepe et al. 2002). A G2V mask was used as it has been highly optimized for RV measurements but also because the spectra have low signal to noise (meaning only the strongest lines are detected). In addition, NGTS-28A is rotating fast, meaning many lines are blended. Fig. 6 shows the time series for the NGTS-28A RV measurements.

The pipeline also produces values for the bisector inverse slope (BIS; Queloz et al. 2001; Dall et al. 2006) which can be an indicator for variability or a blended eclipsing binary (Santos et al. 2002; Günther et al. 2018). The automatic pipeline calculation of the BIS picked up a local minima in the cross-correlation function (CCF) and computed BIS values from that. To mitigate this, we binned the CCF to 5 km s^{-1} in velocity space and re-calculated the BIS. The RV values for NGTS-28B and BIS values for both objects are also in Table 2.

2.3 High-resolution imaging with ZORRO

Nearby companion stars can appear to mimic transit signatures in light curves, as well as affecting the detected depth of any real transiting event meaning the derived radii of any secondary object

Table 3. Magnitudes, parameters, and kinematics of NGTS-28A and NGTS-28B. The kinematics of the two objects are from *Gaia* DR3 and the photometry is from *Gaia* DR3 (Gaia Collaboration 2023), 2MASS (Skrutskie et al. 2006), PanSTARRS (Chambers et al. 2016; Flewelling et al. 2020). The *TESS* magnitude is from ExoFOP (Ricker et al. 2014). We list parameters of NGTS-28A and NGTS-28B found using SPECMATCH-EMP as priors for ARIADNE. Due to the low SNR of the spectra and the blending in photometry available, the errors in the parameters are likely underestimated and represent numerical errors.

Parameter	NGTS-28A	NGTS-28B
Gaia Source ID	6 172969891098581120	6172969891098581248
RA	14:11:43.0	14:11:42.9
Dec.	−29:58:28.39	−29:58:26.32
pmRA (mas yr^{-1})	-78.61 ± 0.02	-79.06 ± 0.04
pmDec (mas yr^{-1})	24.74 ± 0.02	23.77 ± 0.03
Parallax (mas)	8.113 ± 0.020	8.085 ± 0.034
Distance (pc)	123.25 ± 0.31	123.86 ± 0.53
Magnitudes		
Gaia G	14.137 ± 0.001	15.249 ± 0.001
Gaia BP	15.250 ± 0.006	16.550 ± 0.005
Gaia RP	13.088 ± 0.003	14.097 ± 0.002
TESS (*T*)	13.074 ± 0.009	14.064 ± 0.008
$2MASS_J$	11.664 ± 0.039	12.552 ± 0.025
$2MASS_H$	11.057 ± 0.047	11.958 ± 0.038
$2MASS_{Ks}$	10.832 ± 0.037	11.757 ± 0.027
$PanSTARRS_g$	15.623 ± 0.004	16.923 ± 0.007
$PanSTARRS_r$	14.373 ± 0.003	15.716 ± 0.010
$PanSTARRS_i$	n/a	14.568 ± 0.006
Fitted Parameters		
$T_{\rm eff}$ (K)	3626^{+47}_{-44}	3441^{+70}_{-52}
$\log g$ (dex)	$4.74^{+0.10}_{-0.09}$	$4.85^{+0.13}_{-0.14}$
[Fe/H] (dex)	$-0.14^{+0.16}_{-0.17}$	$-0.02^{+0.26}_{-0.23}$
$M_{\rm A}$(M$_\odot$)	$0.56^{+0.02}_{-0.02}$	$0.43^{+0.01}_{-0.02}$
$R_{\rm A}$ (R$_\odot$)	$0.59^{+0.03}_{-0.03}$	$0.42^{+0.03}_{-0.03}$
Age (Gyr)	$6.99^{+5.09}_{-6.49}$	$2.06^{+10.08}_{-1.49}$

Table 4. Estimate Matern-3/2 baseline parameters from ALLESFITTER. These were used as priors within the final fit.

Parameter	NGTS	*TESS*
ln_σ	$-4.6161^{+0.0587}_{-0.0587}$	$-4.4589^{+0.1135}_{-0.1135}$
ln_ρ	$-1.4840^{+0.0764}_{-0.0764}$	$-0.9483^{+0.1049}_{-0.1049}$

will be incorrect (Howell et al. 2011; Furlan & Howell 2017). High-resolution imaging of the host star is one way to determine if the host star is actually an unresolved binary.

We performed speckle imaging with ZORRO on 2023 May 08 (Scott et al. 2021; Howell & Furlan 2022). The resultant 5σ contrast curve can be seen in Fig. 7, where the two filters used (562 nm and 832 nm, blue and red, respectively) are plotted. We obtained 12 sets of 1000 images with an exposure time of 0.06 s, which was processed using the standard pipeline, detailed in Howell et al. (2011).

Fig. 7 shows no nearby stellar companions detected near NGTS-28A to within the contrast (4 mag at 562 nm and 5.8 mag at 832 nm) and the angular separation (0.02–1.2 arcsec) limits of the observation. Meaning we detected no stellar companion between around 2.5 and 147.9 au around NGTS-28A. A reconstructed 832 nm image can be seen in the inset of Fig. 7.

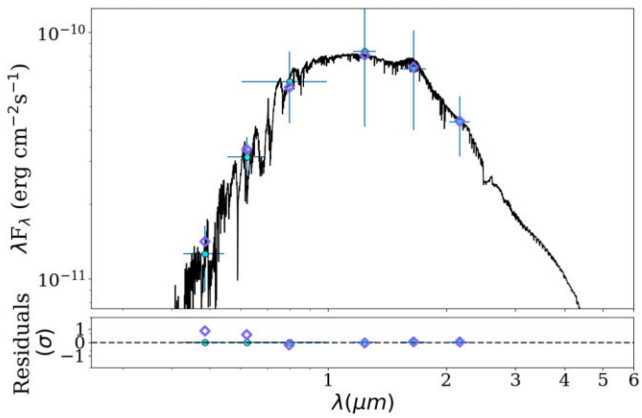

Figure 8. SED fit produced by ARIADNE. Black line shows the PHOENIX V2 model, light blue points show the various catalogue photometry points for NGTS-28A and the purple diamonds show the synthetic photometry fit. Plotted underneath are the residuals for the data and synthetic photometry.

3 ANALYSIS

3.1 NGTS-28B

Fig. 1 shows the DSS image of NGTS-28Ab and shows NGTS-28A is blended with another star (NGTS-28B), with an on sky separation of ∼3.6 arcsec. We compared the *Gaia* DR3 kinematics (Gaia Collaboration 2016, 2023) for NGTS-28B and NGTS-28A

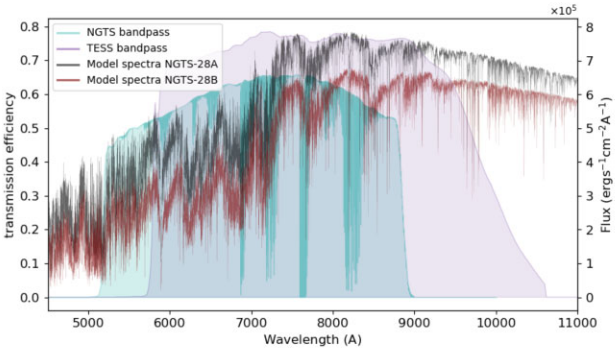

Figure 9. The NGTS bandpass (blue) and *TESS* bandpass (indigo) with NGTS-28A (black) and NGTS-28B (red) model spectra plotted. The NGTS bandpass curve is the product of the quantum efficiency curve of the CCD, the filter transmission curve and an atmospheric absorption curve (Günther et al. 2018; Wheatley et al. 2018). The *TESS* bandpass curve is the product of the filter transmission curve and detector quantum efficiency curve (Ricker et al. 2014).

(Table 3). NGTS-28B has a proper motion and parallax in *Gaia* DR3 that is similar to that of NGTS-28A, although the proper motion is not consistent within the errors. However, Mugrauer, Rück & Michel (2023) have found NGTS-28A and NGTS-28B to be co-moving within their multiplicity study. Combining the distance to NGTS-28A and angular separation (3.6 arcsec) of NGTS-28AB, the separation is ∼443 au. This wide separation also means NGTS-28B will not have any substantial gravitational effect on NGTS-28A, and so will not affect orbital RV measurements for NGTS-28Ab over the time span of the observations taken.

Within 15 arcsec, there is a third object which has a *Gaia G* magnitude of 20.3 (Gaia Collaboration 2023), but it does not have a parallax or proper motion which is consistent with being a common proper motion companion. This object is too faint to have a significant effect on our photometry. We also searched the wider field within 5 arcsec for proper motion companions, but none were found. Within 60 arcsec, there are 18 objects, but none of which are brighter than the host star. It is unlikely any of these objects have a significant contribution to the photometry of the system due to their separation, especially compared to NGTS-28B. NGTS-28B has been taken into consideration within our analysis, as blending within the aperture will affect the depth of the measured transit (Ciardi et al. 2015). This is discussed further in Section 3.3.1.

3.2 NGTS-28A: host star parameters

We analysed NGTS-28A using spectral fitting and spectral energy distribution (SED) fitting. Table 3 gives the proper motion, parallax, and magnitudes from *Gaia* DR3 (Gaia Collaboration 2016, 2023), *TESS*, 2MASS (Skrutskie et al. 2006), and PanSTARRS (Chambers et al. 2016; Flewelling et al. 2020).

3.2.1 *Spectral analysis*

We analysed the HARPS spectra with SPECMATCH-EMP (Yee, Petigura & von Braun 2017) for both NGTS-28A and NGTS-28B. First, we shifted the spectra into the rest frame to remove the RV variations, then co-added the spectra to obtain a single spectrum with a higher signal-to-noise ratio (SNR) than the individual spectra, although the total SNR of the co-added spectrum of NGTS-28A was still low per pixel (5.5). We then used SPECMATCH-EMP to compare our spectra to the KECK/HIRES libraries of template spectra in order to select a few 'best-fitting' objects to the target spectra. Linearly combined spectra of the comparison objects were then created and compared to the target spectra, to get a best fit. The output parameters are calculated using the weighted averages of the linearly combined spectra. SPECMATCH-EMP then uses χ^2 statistics to test how good of a fit the estimated parameters are to the data.

We determined that NGTS-28A has a mass of 0.56 ± 0.08 $M_{\odot}$, radius of 0.53 ± 0.1 $R_{\odot}$, and a $T_{\rm eff}$ of 3630 ± 70 K. We also found it has a log g of 4.74 ± 0.12 and a [Fe/H] of 0.36 ± 0.09. For NGTS-28B, we determined a mass of 0.39 ± 0.08 $M_{\odot}$ radius of 0.39 ± 0.1 $R_{\odot}$ and a $T_{\rm eff}$ of 3500 ± 70 K. We also found a log g of 4.87 ± 0.12 and a [Fe/H] of 0.00 ± 0.09. The errors estimated by SPECMATCH-EMP are likely underestimates due to the low SNR of the spectra, which is not considered within SPECMATCH-EMP. The SPECMATCH-EMP code uses fixed errors for all results, which depend only on the property's value. For example, the $T_{\rm eff}$ will have an adopted error of 70 K if it is less than 4500 K and an adopted error of 110 K if $T_{\rm eff}$ is greater than or equal to 4500 K. For more information, we refer the reader to the software paper (Yee, Petigura & von Braun 2017).

The two objects are of a similar $T_{\rm eff}$ with NGTS-28B being slightly cooler than NGTS-28A. We also find that NGTS-28B is less massive with a smaller radius than NGTS-28A. These values are consistent with NGTS-28B being fainter than NGTS-28A. The age of both objects are also found to be in agreement within errors, supporting that they are likely common proper motion companions. We used the log g, radius, and $T_{\rm eff}$ of NGTS-28A and NGTS-28B as priors for ARIADNE.

3.2.2 *SED fitting*

We fit the broadband photometry in Table 3 for NGTS-28A and NGTS-28B using ARIADNE, a SED fitting tool (Vines & Jenkins 2022) that uses six atmospheric models (PHOENIX: Husser et al. 2013; BT-SETTL: Allard, Homeier & Freytag 2012; BT-NEXTGEN: Hauschildt, Allard & Baron 1999; Allard, Homeier & Freytag 2012; BT-COND: Allard, Homeier & Freytag 2012; CASTELLI & KURUCZ: Castelli & Kurucz 2004; KURUCZ: Kurucz 1993) to determine various stellar parameters.

For NGTS-28A and NGTS-28B, we used $T_{\rm eff}$, radius, and log g from SPECMATCH-EMP as priors for the ARIADNE fit. This produced the values in Table 3. It is likely that these values have slightly underestimated errors due to how blended NGTS-28A and NGTS-28B are in the optical photometry.

The SED for NGTS-28A is shown in Fig. 8 with the PHOENIX V2 model spectra. Synthetic photometry points, and the residuals between the synthetic and real photometry points are also seen in Fig. 8. The data in Table 3 were taken from the Bayesian Model Average output from ARIADNE.

The ages from ARIADNE are in agreement with each other but the errors very large. The mass and radius of NGTS-28B are smaller than NGTS-28A, as expected when compared to SPECMATCH-EMP.

To obtain rough estimates for the spectral types of both NGTS-28A and NGTS-28B, the $T_{\rm eff}$ values were compared to fig. 5 of Rajpurohit et al. (2013). In Rajpurohit et al. (2013)'s figure, the $T_{\rm eff}$ values are plotted with spectral type to show a trend for how $T_{\rm eff}$ values change as you progress to later M dwarf types, along with multiple atmospheric models for comparison. Using the $T_{\rm eff}$ values for NGTS-28A and NGTS-28B, we compared to this figure (Rajpurohit et al. 2013) to estimate a spectral type for both objects. We estimate a spectral type of ∼M1 for NGTS-28A and ∼M2 for NGTS-28B. We compared this to the Mamajek spectral

Table 5. The fitted parameters for NGTS-28Ab, produced by ALLESFITTER.

Parameter	Symbol	Prior, parameter space	Value
		Fitted parameters	
Limb darkening parameters			
NGTS LDC 1	$q_{1;\,\mathrm{NGTS}}$	0.4544, $\mathcal{N}$(0.4544, 0.0088)	$0.4517^{+0.0074}_{-0.0078}$
NGTS LDC 2	$q_{2;\,\mathrm{NGTS}}$	0.2901, $\mathcal{N}$(0.2901, 0.0022)	$0.2900^{+0.0018}_{-0.0019}$
TESS Sector 38 LDC 1	$q_{1;\,\mathrm{TESS}}$	0.3379, $\mathcal{N}$(0.3379, 0.0054)	$0.3383^{+0.0046}_{-0.0043}$
TESS Sector 38 LDC 2	$q_{2;\,\mathrm{TESS}}$	0.2640, $\mathcal{N}$(0.2640, 0.0019)	$0.2638^{+0.0017}_{-0.0017}$
SPECULOOS-S $I+z$’ band LDC 1	$q_{1;\mathrm{SPEC_izp}}$	0.2284, $\mathcal{N}$(0.2284, 0.0037)	$0.2290^{+0.0032}_{-0.0033}$
SPECULOOS-S $I+z$’ band LDC 2	$q_{2;\mathrm{SPEC_izp}}$	0.2199, $\mathcal{N}$(0.2199, 0.0020)	$0.2195^{+0.0016}_{-0.0017}$
SPECULOOS-S z’ band LDC 1	$q_{1;\mathrm{SPEC_zp}}$	0.2015, $\mathcal{N}$(0.2015, 0.0031)	$0.2015^{+0.0026}_{-0.0026}$
SPECULOOS-S z’ band LDC 2	$q_{2;\mathrm{SPEC_zp}}$	0.2027, $\mathcal{N}$(0.2027, 0.0019)	$0.2030^{+0.0016}_{-0.0017}$
SPECULOOS-S g’ band LDC 1	$q_{1;\mathrm{SPEC_gp}}$	0.8945, $\mathcal{N}$(0.8945, 0.0143)	$0.8911^{+0.0118}_{-0.0118}$
SPECULOOS-S g’ band LDC 2	$q_{2;\mathrm{SPEC_gp}}$	0.3271, $\mathcal{N}$(0.3271, 0.0016)	$0.3270^{+0.0014}_{-0.0014}$
SPECULOOS-S i’ band LDC 1	$q_{1;\mathrm{SPEC_ip}}$	0.3531, $\mathcal{N}$(0.3531, 0.0070)	$0.3550^{+0.0059}_{-0.0059}$
SPECULOOS-S i’ band LDC 2	$q_{2;\mathrm{SPEC_ip}}$	0.2678, $\mathcal{N}$(0.2678, 0.0024)	$0.2676^{+0.0020}_{-0.0019}$
SPECULOOS-S r’ band LDC 1	$q_{1;\mathrm{SPEC_rp}}$	0.7794, $\mathcal{N}$(0.7794, 0.0151)	$0.7790^{+0.0127}_{-0.0129}$
SPECULOOS-S r’ band LDC 2	$q_{2;\mathrm{SPEC_rp}}$	0.3161, $\mathcal{N}$(0.3161, 0.0020)	$0.3162^{+0.0018}_{-0.0018}$
TRAPPIST-S $I+z$’ band LDC 1	$q_{1;\mathrm{TRAP_izp}}$	0.2284, $\mathcal{N}$(0.2284, 0.0074)	$0.2293^{+0.0067}_{-0.0062}$
TRAPPIST-S $I+z$’ band LDC 2	$q_{2;\mathrm{TRAP_izp}}$	0.2199, $\mathcal{N}$(0.2199, 0.0040)	$0.2199^{+0.0034}_{-0.0034}$
TRAPPIST-S z’ band LDC 1	$q_{1;\mathrm{TRAP_zp}}$	0.2015, $\mathcal{N}$(0.2015, 0.0062)	$0.2020^{+0.0053}_{-0.0054}$
TRAPPIST-S z’ band LDC 2	$q_{2;\mathrm{TRAP_zp}}$	0.2027, $\mathcal{N}$(0.2027, 0.0038)	$0.2030^{+0.0032}_{-0.0033}$
SAAO I band LDC 1	$q_{1;\mathrm{SAAO_I}}$	0.5, $\mathcal{U}$(0.0, 1.0)	$0.2191^{+0.1091}_{-0.0892}$
SAAO I band LDC 2	$q_{2;\mathrm{SAAO_I}}$	0.5, $\mathcal{U}$(0.0, 1.0)	$0.6158^{+0.2615}_{-0.3336}$
System parameters			
Radius ratio	$R_b/R_\star$	0.116, $\mathcal{U}$(0.0, 0.3)	$0.1667^{+0.0011}_{-0.0010}$
Scaled summed radius	$(R_\star+R_b)/a_b$	0.16,$\mathcal{U}$(0.0, 0.3)	$0.1579^{+0.0027}_{-0.0024}$
Cosine inclination	$\cos i_b$	0, $\mathcal{U}$(0.0, 0.5)	$0.0808^{+0.0032}_{-0.0030}$
Epoch (BJD)	$T_{0;\,b}$	2459360.305123, $\mathcal{U}$(2459350, 2459370)	$2458953.9685^{+0.0001}_{-0.0001}$
Orbital period (d)	P_{orb}	1.25412, $\mathcal{U}$(1.245, 1.265)	$1.2541^{+0.0000}_{-0.0000}$
RV Semi-amplitude (km s^{-1})	K_b	15, $\mathcal{U}$(12, 22)	$18.4107^{+0.2367}_{-0.1659}$
$\sqrt{e_b}\cos\omega_b$	f_c	0, $\mathcal{U}$(−1, 1)	$-0.0289^{+0.0236}_{-0.0173}$
$\sqrt{e_b}\sin\omega_b$	f_s	0, $\mathcal{U}$(−1, 1)	$-0.1981^{+0.0267}_{-0.0156}$
Dilution values			
NGTS dilution	D_{NGTS}	0.4364, $\mathcal{N}$(0.4364, 0.0186)	$0.4222^{+0.0095}_{-0.0111}$
TESS dilution	D_{TESS}	0.4466,$\mathcal{N}$(0.4466, 0.0156)	$0.4145^{+0.0089}_{-0.0097}$
SPECULOOS-S $I+z$’ dilution	$D_{\mathrm{SPEC_izp}}$	–	0.0 (fixed)
SPECULOOS-S z’ dilution	$D_{\mathrm{SPEC_zp}}$	–	0.0 (fixed)
SPECULOOS-S g’ d	$D_{\mathrm{SPEC_gp}}$	–	0.0 (fixed)
SPECULOOS-S i’ dilution	$D_{\mathrm{SPEC_ip}}$	0, $\mathcal{U}$(0, 1)	$0.0226^{+0.0191}_{-0.0145}$
SPECULOOS-S r’ dilution	$D_{\mathrm{SPEC_rp}}$	–	0.0 (fixed)
TRAPPIST-S $I+z$’ dilution	$D_{\mathrm{TRAP_izp}}$	0, $\mathcal{U}$(0, 1)	$0.3599^{+0.0268}_{-0.0265}$
TRAPPIST-S z’ dilution	$D_{\mathrm{TRAP_zp}}$	0, $\mathcal{U}$(0, 1)	$0.3648^{+0.0268}_{-0.0262}$
SAAO I-band dilution	$D_{\mathrm{SAAO_I}}$	0, $\mathcal{U}$(0, 1)	$0.1791^{+0.0276}_{-0.0269}$
White noise			
–	$\ln\sigma_{\mathrm{NGTS}}$	−5, $\mathcal{U}$(−10, −1)	$-5.0915^{+0.0073}_{-0.0073}$
–	$\ln\sigma_{\mathrm{TESS}}$	−5, $\mathcal{U}$(−10, −1)	$-5.1962^{+0.0081}_{-0.0078}$
–	$\ln\sigma_{\mathrm{SPEC_izp}}$	−5, $\mathcal{U}$(−10, −1)	$-5.5845^{+0.0230}_{-0.0231}$
–	$\ln\sigma_{\mathrm{SPEC_zp}}$	−5, $\mathcal{U}$(−10, −1)	$-5.6716^{+0.0334}_{-0.0328}$
–	$\ln\sigma_{\mathrm{SPEC_gp}}$	−5, $\mathcal{U}$(−10, −1)	$-5.6037^{+0.0672}_{-0.0617}$
–	$\ln\sigma_{\mathrm{SPEC_ip}}$	−5, $\mathcal{U}$(−10, −1)	$-5.2349^{+0.0304}_{-0.0304}$
–	$\ln\sigma_{\mathrm{SPEC_rp}}$	−5, $\mathcal{U}$(−10, −1)	$-5.6961^{+0.0429}_{-0.0435}$
–	$\ln\sigma_{\mathrm{TRAP_izp}}$	−5, $\mathcal{U}$(−10, −1)	$-5.4060^{+0.0345}_{-0.0335}$
–	$\ln\sigma_{\mathrm{TRAP_zp}}$	−5, $\mathcal{U}$(−10, −1)	$-5.6070^{+0.0433}_{-0.0411}$

Table 5 – *continued*

Parameter	Symbol	Prior, parameter space	Value
–	$\ln \sigma_{\mathrm{SAAO_I}}$	$-5, \mathcal{U}(-10, -1)$	$-4.6564^{+0.0174}_{-0.0172}$
–(km s^{-1})	$\ln \sigma_{\mathrm{jitter}}\,(RV_{\mathrm{HARPS}})$	$-2, \mathcal{U}(-4, -1)$	$-2.1615^{+0.5819}_{-0.6698}$
Baseline parameters for GP			
$\ln \sigma_{NGTS}$	offset (NGTS)	$-4.6161, \mathcal{N}(-4.6161, 0.0587)$	$-4.5927^{+0.0386}_{-0.0359}$
$\ln \rho_{NGTS}$	offset (NGTS)	$-1.4840, \mathcal{N}(-1.4840, 0.0764)$	$-1.6515^{+0.0497}_{-0.0577}$
$\ln \sigma_{TESS}$	offset (TESS)	$-4.4589, \mathcal{N}(-4.4589, 0.1135)$	$-4.4356^{+0.0633}_{-0.0582}$
$\ln \rho_{TESS}$	offset (TESS)	$-0.9483, \mathcal{N}(-0.9483, 0.1049)$	$-0.9319^{+0.0697}_{-0.0678}$

types (Pecaut & Mamajek 2013) that were estimated with ARIADNE. ARIADNE estimates a M1.5 and M3 spectral classification for NGTS-28A and NGTS-28B, respectively. Comparing the results from both these methods provides a good estimate for the spectral type of both stars. Although more detailed methods can be used, they are not necessary for understanding NGTS-28Ab, and are limited by the low signal-to-noise spectra that are available.

3.3 NGTS-28Ab Parameters

Due to the complexity of the system, NGTS-28Ab's parameters involved a multistep process to get the most accurate results possible. NGTS-28Ab was analysed using ALLESFITTER (Günther & Daylan 2019, 2021). ALLESFITTER is a statistical tool used to fit light curve and RV data to produce estimations for parameters of the system (Günther & Daylan 2019, 2021). It utilizes MCMC and dynamic nested sampling (DNS) methods to estimate the best fitting parameters to the data, which can simultaneously be provided from multiple instruments and bandpasses, making use of various software including models such as ELLC (Maxted 2016) and samplers such as DYNESTY (Speagle 2020) and EMCEE (Foreman-Mackey et al. 2013).

3.3.1 Estimating dilution values

The first step involved calculating estimates for the dilution values for each instrument. We do this in a similar manner to Günther et al. (2018). To do this, we used PYSYNPHOT (STScI Development Team 2013). We first obtained the bandpass response function for NGTS and *TESS* (NGTS: Günther et al. 2018; Wheatley et al. 2018; *TESS*: Ricker et al. 2014). We then obtained model spectra for both NGTS-28A and NGTS-28B using the PHOENIX models (Husser et al. 2013) within PYSYNPHOT. We randomly sampled 10 000 T_{eff} values between the errors of each object's T_{eff}, which created 10 000 possible spectra for each object.

The bandpass functions for each instrument and an example model spectra for each object produced by the PHOENIX models are plotted in Fig. 9. Once we had obtained these, we interpolated the bandpass and spectra, multiplied the stellar spectra by the transmission curve and then integrated over the entire region. This provided flux values for NGTS-28A and NGTS-28B which could be used in equations (1) and (2) from Günther et al. (2018) to calculate the dilution for NGTS-28A. D_B and D_A are the dilution values for NGTS-28B and NGTS-28A, respectively. F_B and F_A are the flux values for NGTS-28B and NGTS-28A, respectively.

$$D_B = 1 - \frac{F_B}{F_A + F_B} \quad (1)$$

$$D_A = 1 - D_B \quad (2)$$

The dilutions were calculated for each of the 10 000 spectra, and a mean was calculated. To estimate the error on this value we also calculated a standard deviation for the sample. From this we determined that NGTS-28A has a dilution value of 0.4364 ± 0.0186 and 0.4466 ± 0.0156 in NGTS and *TESS*, respectively. *TESS* PDCSAP estimated a dilution of 0.73 which is larger than the modelled dilution for NGTS-28A or NGTS-28B. This confirmed that the PDCSAP flux has likely been over corrected for this object.

3.3.2 Global modelling

For the global modelling of the system, we modelled the *TESS* 2-min cadence data, the NGTS data which we binned to 2-min, the SAAO, SPECULOOS-S, and TRAPPIST-S data sets and the HARPS RV data simultaneously using ALLESFITTER. We removed some data in the SAAO *I*-band data due to variable seeing but kept in as much as possible. We also remove some data from the SPECULOOS-S g' and r' due to high background noise.

We estimated the baseline parameters ln_σ and ln_ρ for NGTS and *TESS*, which describe a GP baseline with a Matern-3/2 kernel, as seen in Günther & Daylan (2021), using the 'out of transit' data in the light curve. These were used as priors for the final fit on the in-transit data, varying normally with their errors (Table 4). HARPS was fit with a hybrid offset and the rest of the photometric data sets were fit with hybrid splines.

For the dynamic nested sampling (DNS) fitting, we fixed the dilution for SPECULOOS-S $I + z'$, g', r' and z' to 0 due to there not being any contamination within the aperture. We used the dilution values for NGTS and *TESS* for NGTS-28A from Section 3.3.1 as priors for the fit, and allowed them to vary normally within their errors. For all other data sets we used an initial prior of 0 and allowed it to vary uniformly between 0 and 1. We did not calculate dilution values due to the method of photometry described in Sections 2.1.3–2.1.5.

The limb darkening values for *TESS*, NGTS, and all SPECULOOS-S and TRAPPIST-S data were calculated using LDTK (Husser et al. 2013; Parviainen & Aigrain 2015), using the Kipping (2013) limb darkening relations. These were fitted with a normal distribution around the priors within the errors produced by LDTK. For SAAO *I* data, the limb darkening constants had initial priors of 0.5, varying uniformly between 0 and 1.

All priors, their parameter spaces and resultant values can be seen in Table 5. The epoch is given a prior value and parameter space but is allowed to shift in order to prevent biasing towards one data set which would cause correlations between epoch and period. We used 500 live points and a tolerance of 0.001. We fit the data with a 0.4 phase width around the transit.

The derived parameters are in Table 6. The corner plot for the derived values from this fit are also in the appendix in Fig. A1. Plots

Table 6. The final DNS derived parameters for NGTS-28Ab, produced by ALLESFITTER. These values are used in future analysis.

Parameter	Value
Derived parameters	
Host radius over semi-major axis b; $R_\star/a_\mathrm{b}$	$0.1353^{+0.0023}_{-0.0020}$
Semi-major axis b over host radius; $a_\mathrm{b}/R_\star$	$7.3872^{+0.1127}_{-0.1210}$
Companion radius b over semimajor axis b; $R_\mathrm{b}/a_\mathrm{b}$	$0.0226^{+0.0005}_{-0.0004}$
Companion radius b; R_b ($\mathrm{R_{jup}}$)	$0.9534^{+0.0488}_{-0.0484}$
Semimajor axis b; a_b ($\mathrm{R_\odot}$)	$4.3387^{+0.2313}_{-0.2282}$
Semimajor axis b; a_b (au)	$0.0202^{+0.0011}_{-0.0011}$
Inclination b; i_b (deg)	$85.3628^{+0.1735}_{-0.1863}$
Eccentricity b; e_b	$0.0404^{+0.0067}_{-0.0101}$
Argument of periastron b; w_b (deg)	$261.7232^{+6.7190}_{-4.9514}$
Mass ratio b; q_b	$0.1181^{+0.0077}_{-0.0069}$
Companion mass b; M_b ($\mathrm{M_{jup}}$)	$69.0125^{+5.3172}_{-4.8181}$
Companion mass b; M_b ($\mathrm{M_\odot}$)	$0.0659^{+0.0051}_{-0.0046}$
Impact parameter b; $b_\mathrm{tra;\,b}$	$0.6200^{+0.0147}_{-0.01367}$
Total transit duration b; $T_\mathrm{tot;\,b}$ (h)	$1.3404^{+0.0105}_{-0.0093}$
Full-transit duration b; $T_\mathrm{full;\,b}$ (h)	$0.7537^{+0.0117}_{-0.0135}$
Host density from orbit b; $\rho_{\star;\,\mathrm{b}}$ (cgs)	$4.8485^{+0.2253}_{-0.2344}$
Companion density b; ρ_b (cgs)	$98.7270^{+23.9807}_{-18.6470}$
Companion surface gravity b; g_b (cgs)	$210796.5463^{+7782.8359}_{-8754.0340}$
Equilibrium temperature b; $T_\mathrm{eq;\,b}$ (K)	$863.2442^{+13.1585}_{-12.5882}$
Transit depth (undil.) b; $\delta_\mathrm{tr;undil;b;NGTS_2}$ (ppt)	$30.2106^{+0.7684}_{-0.7502}$
Transit depth (dil.) b; $\delta_\mathrm{tr;dil;b;NGTS_2}$ (ppt)	$17.4391^{+0.3714}_{-0.2668}$
Transit depth (undil.) b; $\delta_\mathrm{tr;undil;b;TESS_2MIN}$ (ppt)	$29.8102^{+0.6466}_{-0.6463}$
Transit depth (dil.) b; $\delta_\mathrm{tr;dil;b;TESS_2MIN}$ (ppt)	$17.4538^{+0.2612}_{-0.2484}$
Transit depth (undil.) b; $\delta_\mathrm{tr;undil;b;SPEC1506_izp}$ (ppt)	$29.4026^{+0.3149}_{-0.3047}$
Transit depth (dil.) b; $\delta_\mathrm{tr;dil;b;SPEC1506_izp}$ (ppt)	$29.4026^{+0.3149}_{-0.3047}$
Transit depth (undil.) b; $\delta_\mathrm{tr;undil;b;SPEC1506_zp}$ (ppt)	$29.2768^{+0.3060}_{-0.3085}$
Transit depth (dil.) b; $\delta_\mathrm{tr;dil;b;SPEC1506_zp}$ (ppt)	$29.2768^{+0.3060}_{-0.3085}$
Transit depth (undil.) b; $\delta_\mathrm{tr;undil;b;SPEC1804_gp_short}$ (ppt)	$31.5803^{+0.3587}_{-0.3317}$
Transit depth (dil.) b; $\delta_\mathrm{tr;dil;b;SPEC1804_gp_short}$ (ppt)	$31.5803^{+0.3587}_{-0.3317}$
Transit depth (undil.) b; $\delta_\mathrm{tr;undil;b;SPEC1804_ip}$ (ppt)	$29.8533^{+0.7533}_{-0.6928}$
Transit depth (dil.) b; $\delta_\mathrm{tr;dil;b;SPEC1804_ip}$ (ppt)	$29.1418^{+0.4886}_{-0.5315}$
Transit depth (undil.) b; $\delta_\mathrm{tr;undil;b;SPEC1804_rp_short}$ (ppt)	$31.2219^{+0.3354}_{-0.3301}$
Transit depth (dil.) b; $\delta_\mathrm{tr;dil;b;SPEC1804_rp_short}$ (ppt)	$31.2219^{+0.3354}_{-0.3301}$
Transit depth (undil.) b; $\delta_\mathrm{tr;undil;b;TRAP1804_izp}$ (ppt)	$29.3713^{+1.7601}_{-1.6165}$
Transit depth (dil.) b; $\delta_\mathrm{tr;dil;b;TRAP1804_izp}$ (ppt)	$18.7979^{+0.7569}_{-0.7499}$
Transit depth (undil.) b; $\delta_\mathrm{tr;undil;b;TRAP2903_zp}$ (ppt)	$29.3008^{+1.7784}_{-1.6831}$
Transit depth (dil.) b; $\delta_\mathrm{tr;dil;b;TRAP2903_zp}$ (ppt)	$18.5946^{+0.8035}_{-0.7835}$
Transit depth (undil.) b; $\delta_\mathrm{tr;undil;b;SAAO_Is}$ (ppt)	$29.4383^{+1.4229}_{-1.3570}$
Transit depth (dil.) b; $\delta_\mathrm{tr;dil;b;SAAO_Is}$ (ppt)	$24.2032^{+0.7457}_{-0.8746}$
Limb darkening; $u_\mathrm{1;NGTS_2}$	$0.3897^{+0.0045}_{-0.0045}$
Limb darkening; $u_\mathrm{2;NGTS_2}$	$0.2823^{+0.0033}_{-0.0035}$
Limb darkening; $u_\mathrm{1;TESS_2MIN}$	$0.3069^{+0.0029}_{-0.0029}$
Limb darkening; $u_\mathrm{2;TESS_2MIN}$	$0.2748^{+0.0027}_{-0.0028}$
Limb darkening; $u_\mathrm{1;SPEC1506_izp}$	$0.2100^{+0.0022}_{-0.0022}$
Limb darkening; $u_\mathrm{2;SPEC1506_izp}$	$0.2684^{+0.0026}_{-0.0026}$
Limb darkening; $u_\mathrm{1;SPEC1506_zp}$	$0.1822^{+0.0019}_{-0.0020}$
Limb darkening; $u_\mathrm{2;SPEC1506_zp}$	$0.2666^{+0.0024}_{-0.0023}$
Limb darkening; $u_\mathrm{1;SPEC1804_gp_short}$	$0.6173^{+0.0053}_{-0.0050}$
Limb darkening; $u_\mathrm{2;SPEC1804_gp_short}$	$0.3265^{+0.0034}_{-0.0033}$

Table 6 – *continued*

Parameter	Value
Limb darkening; $u_{1;\mathrm{SPEC1804_{i}p}}$	$0.3188^{+0.0038}_{-0.0035}$
Limb darkening; $u_{2;\mathrm{SPEC1804_{i}p}}$	$0.2768^{+0.0035}_{-0.0035}$
Limb darkening; $u_{1;\mathrm{SPEC1804_{r}p_{s}hort}}$	$0.5583^{+0.0054}_{-0.0057}$
Limb darkening; $u_{2;\mathrm{SPEC1804_{r}p_{s}hort}}$	$0.3244^{+0.0044}_{-0.0042}$
Limb darkening; $u_{1;\mathrm{TRAP1804_{i}zp}}$	$0.2107^{+0.0048}_{-0.0049}$
Limb darkening; $u_{2;\mathrm{TRAP1804_{i}zp}}$	$0.2682^{+0.0047}_{-0.0046}$
Limb darkening; $u_{1;\mathrm{TRAP2903_{z}p}}$	$0.1823^{+0.0042}_{-0.0039}$
Limb darkening; $u_{2;\mathrm{TRAP2903_{z}p}}$	$0.2668^{+0.0047}_{-0.0045}$
Limb darkening; $u_{1;\mathrm{SAAO_{I}s}}$	$0.5458^{+0.2411}_{-0.2874}$
Limb darkening; $u_{2;\mathrm{SAAO_{I}s}}$	$-0.1005^{+0.3080}_{-0.2210}$

showing the model fits to the various sources of data can be seen in Figs 10 and 11.

The radius of NGTS-28Ab was therefore found to be 0.95 ± 0.05 R_J, with a mass of $69.0^{+5.3}_{-4.8}$ M_J. These clearly put NGTS-28Ab within the BD regime. The derived eccentricity is $0.0404^{+0.0067}_{-0.0101}$, meaning the orbit is close to circular, but still has some eccentricity.

In order to test if the eccentricity is significant, we repeated the model fit with the eccentricity parameters ($\sqrt{e_b}\cos\omega_b$ and $\sqrt{e_b}\sin\omega_b$) fixed to 0, which fixes the eccentricity of the system to 0. We kept all other priors and parameter spaces the same.

Using the Bayesian evidence calculated during the DNS fit for both the eccentric and circular model, we calculate a logarithmic Bayes factor of 4.5. Using the criteria from Jeffreys (1998) and Kass & Raftery (1995), this means there is strong evidence for the eccentricity to be a significant measurement, but not definitive. However, due to the Bayes factor being close to the limit of decisive (greater than 4.6), and the fact there is still strong evidence for some level of eccentricity, we assume the eccentric model to be the most likely. We perform other tests within Section 4.3 of this paper.

4 DISCUSSION

4.1 Population comparisons: bridging the gap

NGTS-28Ab has a mass of $69.0^{+5.3}_{-4.8}$ M_J and a radius of 0.95 ± 0.05 R_J, putting it at the upper boundary of the BD regime. The small radius also suggests that it is a BD, as most M-dwarfs are predicted by model isochrones to have radii above this value, although there is often a large scatter in the radii of late M-dwarfs (e.g. Parsons et al. 2018). Fig. 12 shows the mass–radius plot for known transiting objects within 12–150 M_J, along with the Baraffe et al. (2003, 2015) isochrones for 0.1, 0.5, 1, 5, and 10 Gyr ages. Objects plotted within Fig. 12 are shown in Table A1. Fig. 12 and Table A1 have been adapted and updated from Grieves et al. (2021). RIK 72B (David et al. 2019) and 2MASS J05352184–0546085 (Stassun, Mathieu & Valenti 2006) are not included within this distribution due to their youth and hence large radii.

Fig.12 shows NGTS-28Ab (plotted as the black triangle) clearly lies within the BD regime, with a system mass ratio of $0.1181^{+0.0069}_{-0.0077}$. Bowler, Blunt & Nielsen (2020) discuss the population statistics of BDs and hot Jupiters, splitting them based on mass and mass ratio. They found that high-mass ratios (greater than 0.01) are more likely to have high eccentricities and indicate stellar formation mechanisms (Bowler, Blunt & Nielsen 2020). The high-mass ratio of this system would make NGTS-28Ab more likely to have formed via stellar formation mechanisms.

NGTS-28Ab sits between the 0.5 and 1 Gyr isochrones on Fig. 12. Although this is in agreement with the ages from SED modelling of NGTS-28A and NGTS-28B within errors, the large range of ages estimated for the system indicate it has a likely age range of >0.5 Gyr.

Low-mass M dwarfs have a wide distribution of radii at the low-mass end with Parsons et al. (2018) determining that only 25 per cent of the M dwarfs they observed had radii consistent with models, while 12 per cent were inflated. It is not yet known whether this scatter continues into the BD regime, although the recent discovery of high-mass inflated BDs indicates it may very well do (e.g. Casewell et al. 2020b; Acton et al. 2021; Schaffenroth et al. 2021).

We determined the metallicity of NGTS-28A using SPECMATCH-EMP and ARIADNE, determining a value of [Fe/H] = $-0.14^{+0.16}_{-0.17}$. Fig. A2 shows the mass and metallicity of the known late M dwarf and BD systems in Table A1. NGTS-28Ab is not an outlier in metallicity within the population for BDs and low-mass stars.

Using ARIADNE, we determined an effective temperatures of 3626^{+47}_{-44} K for NGTS-28A and 3441^{+70}_{-52} K for NGTS-28B. NGTS-28B has a lower temperature than NGTS-28A and it is a redder object. Both objects have early M spectral types. Fig. A3 shows the distribution of objects from Table A1 based on effective temperature. It also shows there is a lack of closely transiting objects around K dwarfs, with NGTS-28A as one of the hottest M Dwarf hosts to transiting BDs, lying close to this gap. A similar gap is seen with eclipsing binaries, where tidal forces cause the companions of K-type stars to spiral inward, as discussed in Chaturvedi et al. (2018).

4.2 Rotation and age

As stated, Fig. 12 shows NGTS-28Ab has mass and radius values which are consistent with the 0.5–1 Gyr isochrone from Baraffe et al. (2003, 2015). This is also consistent with the age estimates of NGTS-28A from ARIADNE. A range of ages is not unexpected due to the difficulty in determining ages of low mass stars. Other checks we performed to test the age of the system are discussed in this section.

We performed a check to confirm whether NGTS-28A and NGTS-28B are part of a known young cluster or association. The BANYAN $\sum$ online tool (Gagné et al. 2018) was used. BANYAN $\sum$ uses RA, Dec., proper motions, and parallax to calculate cluster membership probabilities for various young clusters (up to 800 Myr) within 150 pc, as well as the probability of the object being field age (∼5 Gyr). For both stars, BANYAN $\sum$ estimates a 99.9 per cent

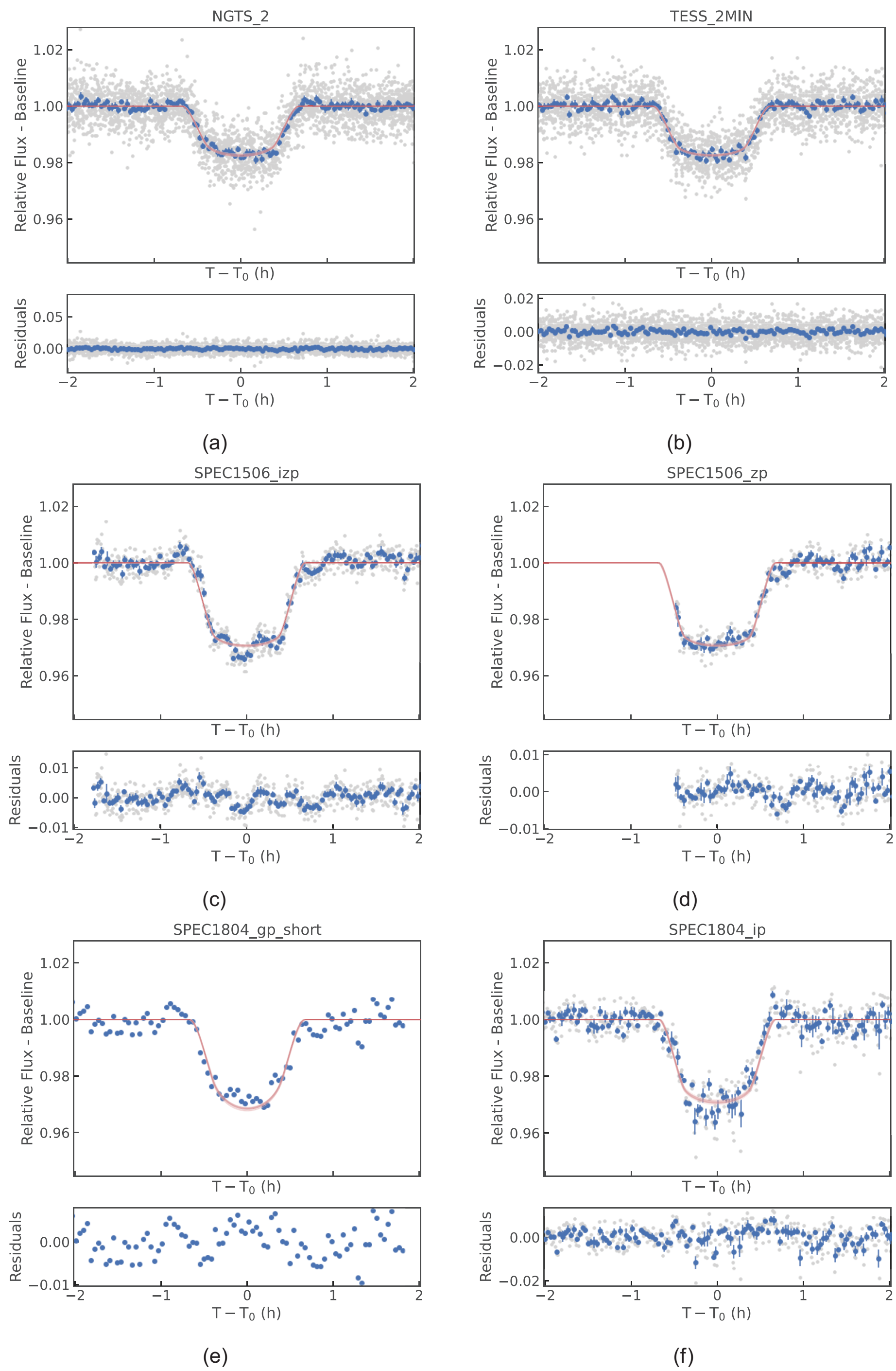

Figure 10. Model fits to (a) NGTS data (binned to 2 min), (b) *TESS* 2 min data, (c) SPECULOOS-S $I + z'$ band data, (d) SPECULOOS-S z' band data, (e) SPECULOOS-S g' band data, (f) SPECULOOS-S i' band data. All model plots are produced with ALLESFITTER. All plots show the inputted data in grey and the 'phased average' flux in blue, with 20 model lines sampled from the posterior.

probability of their being field objects, and are therefore unlikely to be members of young clusters. This high probability of both NGTS-28A and NGTS-28B being field age is consistent with the estimates from ARIADNE.

Another check for youth is whether NGTS-28Ab is in spin-orbit sychronization with NGTS-28A. Spin-orbit synchronization is expected for an object of this orbital radius/period. Fig. 4 shows the full *TESS* data for NGTS-28AB in the top panel. From the bottom of Fig. 4, an apparent signature due to rotation can be seen, along with the transits and a flare. If it is believed to be the rotation of NGTS-28A alone, it appears the rotation period of the object is very close to, but not quite equal to, the orbital period of NGTS-28Ab. However, it is likely that the light curve modulation shows a composite effect of both NGTS-28A and NGTS-28B.

From the large uncertainties in the ages and the high probability of the objects being field age, it is likely that NGTS-28Ab is old.

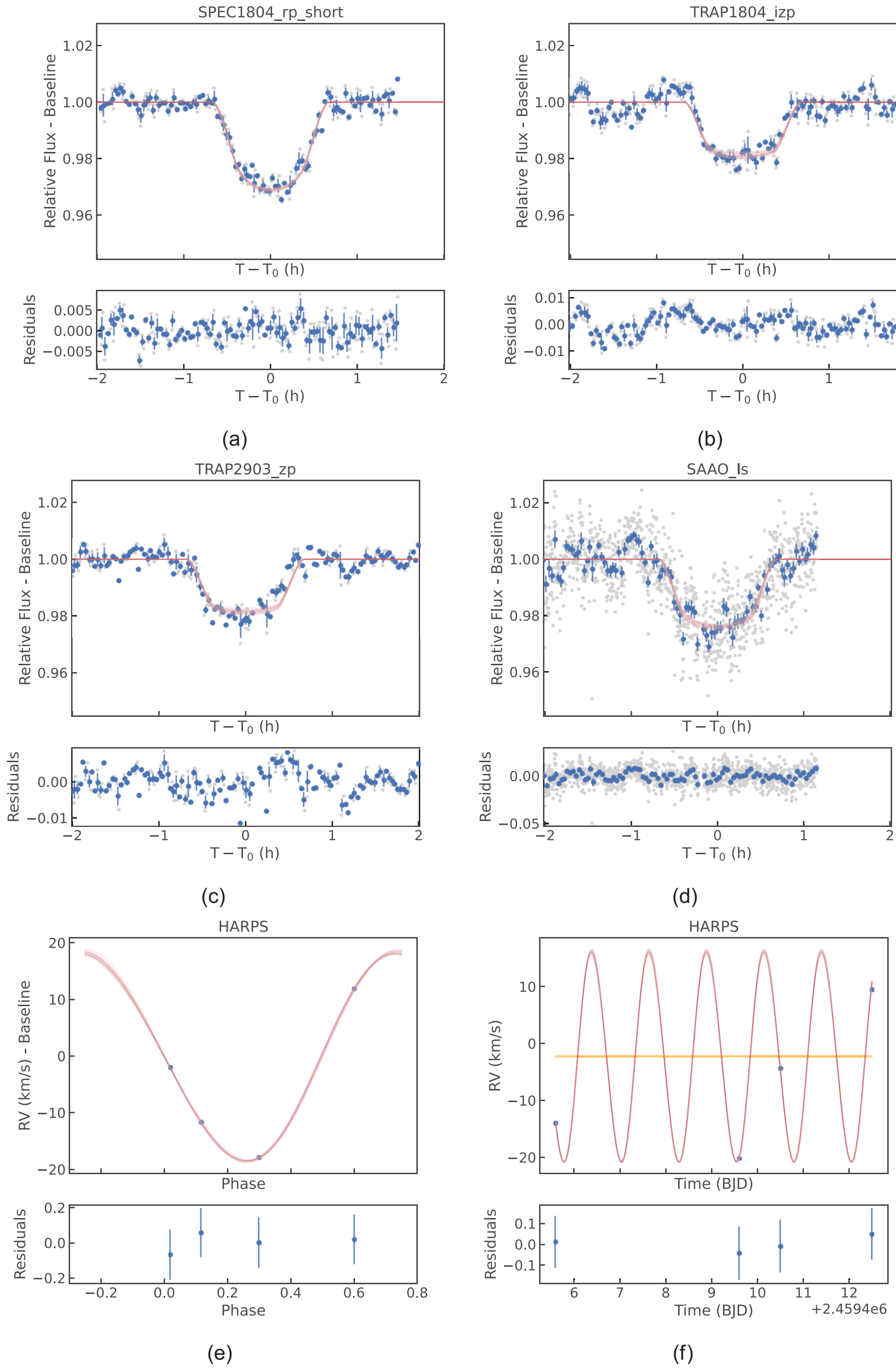

Figure 11. Model fits to (a) SPECULOOS-S r' band data, (b) TRAPPIST-S $I + z'$ band data, (c) TRAPPIST-S z' band data, (d) SAAO I-band data, (e) phase-folded HARPS data, and (f) timeseries HARPS data. All model plots are produced with ALLESFITTER. All plots show the inputted data in grey and the 'phased average' flux in blue, with 20 model lines sampled from the posterior.

If we make the assumption that the modulation seen in the *TESS* and NGTS data is from NGTS-28A alone, we can calculate the rotation period using a Lomb–Scargle (LS) periodogram (Lomb 1976; Scargle 1982). We used ASTROPY's LOMBSCARGLE package (ASTROPY: Astropy Collaboration 2013, 2018, 2022), using a period range between 0.9 and 2 d. The errors associated with the period were calculated by randomly sampling the time-flux array for *TESS* and NGTS, allowing for duplication of values, and repeating the LS process for each random sample, known as 'bootstrapping'. We repeated the process 1000 times and the standard deviation of the resultant periods was used as the error on the period. We determined the rotation period to be 1.42 ± 0.02 d from the *TESS* data and 1.42 ± 0.11 d from the NGTS data. Unfortunately, due to the high level of blending in the photometry from *TESS* and NGTS, we are unable to conclusively say if this rotation period of NGTS-28A is accurate or is a modulation effect caused by the blended

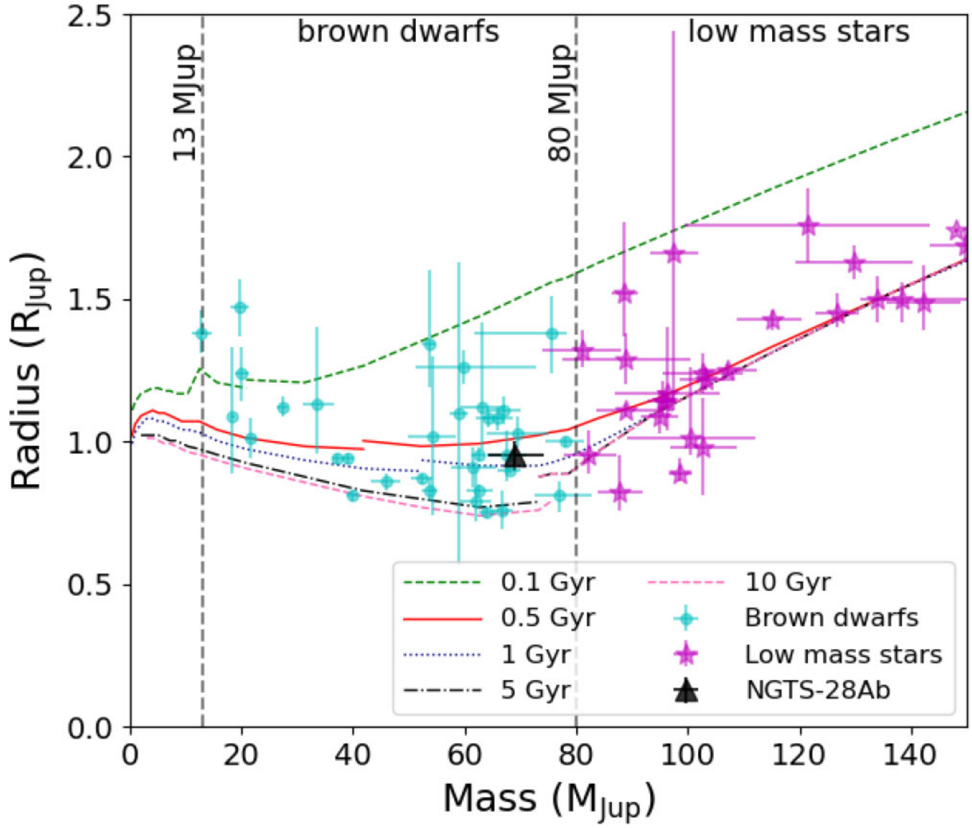

Figure 12. Mass–radius plot for the known transiting BDs (blue circles) and low-mass stars (magenta stars), with NGTS-28Ab (black triangle), adapted from fig. 10 in Grieves et al. (2021). The vertical dashed lines show the upper and lower boundaries of the BD regime. The lines plotted along the graph show the expected radii of objects at all masses for 0.1 Gyr (green dashed), 0.5 Gyr (red solid), 1 Gyr (blue dotted), 5 Gyr (black dash–dotted), and 10 Gyr (pink dashed) objects. These isochrones are from Baraffe et al. 2003, 2015. The Baraffe et al. (2003) isochrones are based on the BT-COND models and Baraffe et al. (2015) improve on that with the inclusion of BT-SETTL models (Allard, Homeier & Freytag 2012). The lowest masses of the isochrones are taken from Baraffe et al. (2003). The disconnect in the isochrone lines is due to using the both models. Objects on this plot are listed within Table A1. RIK-72b (David et al. 2019) and the binary system discovered by Stassun, Mathieu & Valenti (2006) are not included due to their youth and large radii.

Table 7. Estimated values for tidal circularization time-scale for NGTS-28Ab. These values show a range of possible time-scales for Q_b values from $10^{4.5}$ to 10^6.

Q_b	τ_e (Myr)
$10^{4.5}$	0.96
$10^{4.75}$	0.97
10^5	0.98
$10^{5.25}$	0.99
$10^{5.5}$	0.99
$10^{5.75}$	0.99
10^6	1.00

NGTS-28B. This uncertainty means we cannot use this rotation period for gyrochronology or to determine any level of spin-orbit synchronization accurately. Therefore, the mass–radius relation and ARIADNE is used to provide a best estimate for the age of NGTS-28Ab of >0.5 Gyr.

4.3 System eccentricity and tidal effects

The eccentricity of NGTS-28Ab is $0.0404^{+0.0067}_{-0.0101}$. To test if the eccentricity is a significant detection, we use the method from Lucy & Sweeney (1971), where the detected eccentricity is only significant if the eccentricity value is $2.45\sigma_e$ above the errors:

$$e = \hat{e}, \text{ if } \hat{e} > 2.45\sigma_e, \tag{3}$$

$$e = 0, \text{ if } \hat{e} \leq 2.45\sigma_e, \tag{4}$$

Where $\hat{e}$ is estimated eccentricity and σ_e is the standard error on the value. Using this relationship from Lucy & Sweeney (1971), our eccentricity is a significant detection.

We expect NGTS-28Ab to be circularized when considering the tidal circularization time-scale. Tidal circularization is where tidal interactions between a star and its companion cause the orbit to become less eccentric, first discussed in Zahn & Bouchet (1989). From there, objects then undergo rotational and orbital synchronization. To calculate an estimate for the circularization time-scale, we use equations (5), (6), and (7) from Jackson, Greenberg & Barnes (2008).

$$\frac{1}{\tau_{circ,\star}} = \frac{171}{16}\sqrt{\frac{G}{M_\star}}\frac{R_\star^5 M_b}{Q_\star}a^{\frac{-13}{2}}, \tag{5}$$

$$\frac{1}{\tau_{circ,b}} = \frac{63}{4}\frac{\sqrt{GM_\star^3}R_b^5}{Q_b M_b}a^{\frac{-13}{2}}, \tag{6}$$

$$\frac{1}{\tau_e} = \frac{1}{\tau_{circ,\star}} + \frac{1}{\tau_{circ,b}}, \tag{7}$$

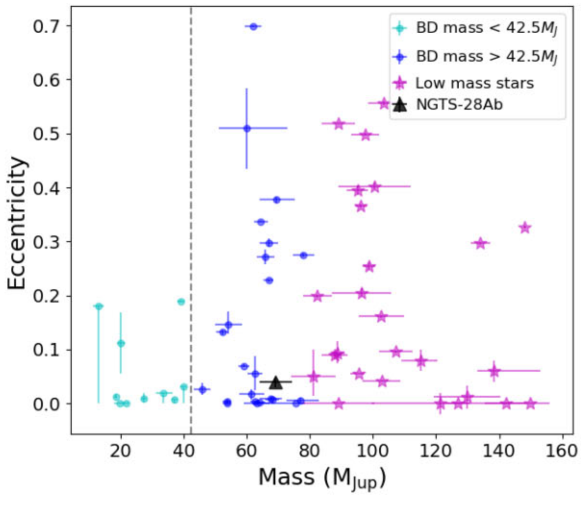

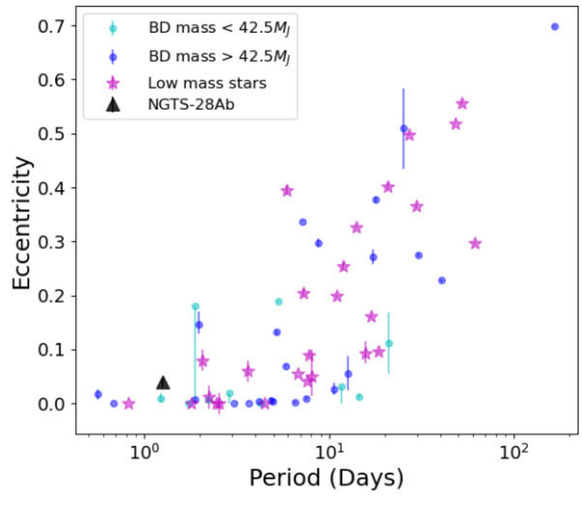

Figure 13. (a) Mass–eccentricity plot, with a vertical dashed line marking 42.5 M_J. (b) Period–eccentricity plot. Both figures show the objects from Table A1 with NGTS-28Ab plotted as an black triangle. Low-mass stars are plotted as magenta stars. BDs with masses above 42.5 M_J are dark blue circles and BDs with below 42.5 M_J are light blue circles. RIK-72b (David et al. 2019) and the binary system discovered by Stassun, Mathieu & Valenti (2006) are not included due to their youth.

Where $\tau_{\mathrm{circ},\star}$, $\tau_{\mathrm{circ},b}$, and τ_e are the circularization time-scales for the star, companion, and system respectively. G is the gravitational constant, $M_\star$ and M_b are the masses of the star and companion respectively, a is the orbital radius and $Q_\star$ and Q_b are the tidal quality factors. This will estimate a circularization time-scale with assumptions such as the orbit is not tidally locked, having a period less than 10 d and the eccentricity being low (Jackson, Greenberg & Barnes 2008).

Using our results and a value of 10^5 for $Q_\star$ (as suggested for M dwarfs in Mardling & Lin 2004; Heller et al. 2010; Heller, Leconte & Barnes 2011), we estimated the circularization timescale for NGTS-28Ab for a range of Q_b values ($10^{4.5}$–10^6) following the methods in Carmichael et al. (2020) and Acton et al. (2021). We use a range of values as the tidal quality factor is not well constrained for BDs. The results can be seen in Table 7. From this test, NGTS-28Ab should have a circularized orbit due to the low time-scales, regardless of Q_b value. This is in disagreement to our significant eccentricity detection. With more RV points we may be able to confirm whether the eccentricity is real.

How the object sits within the BD/low-mass star population is important. Fig. 13, shows the mass-eccentricity relation for all objects from Table A1. In Fig. 13, the objects that are more massive than 42.5 M_J (shown by the dotted line) show a flat eccentricity distribution with increasing mass. This is in agreement with Ma & Ge (2014) and Grieves et al. (2017). NGTS-28Ab lies comfortably within this flat distribution.

From the period-eccentricity plot in Fig. 13, it is clear that objects with the highest eccentricities also tend to have long periods. NGTS-28Ab is one of the shortest period transiting BDs within the desert.

5 CONCLUSION

NGTS-28Ab is a $69.0^{+5.3}_{-4.8}$ M_J, 0.95 ± 0.05 R_J BD, transiting within the sparsely populated BD desert (Grether & Lineweaver 2006). Therefore, NGTS-28Ab provides a new opportunity to gain a deeper understanding of this region. The BD desert is believed to be caused by the minimal overlap of the tail of distributions between planetary and stellar formation mechanisms (Ma & Ge 2014; Grieves et al. 2021). Therefore, it is important to model parameters that can indicate the formation of each object.

We used spectral fitting and SED fitting methods to analyse the host star NGTS-28A as well as the probable common proper motion companion NGTS-28B (Mugrauer, Rück & Michel 2023). We were then able to use the global modelling method ALLESFITTER (Günther & Daylan 2019, 2021) to model the parameters of NGTS-28Ab. Through this we found NGTS-28Ab is likely to have an age >0.5 Gyr and has a high mass ratio of $0.1181^{+0.0069}_{-0.0077}$, meaning it likely formed via stellar formation mechanisms, with a low eccentricity value of $0.0404^{+0.0067}_{-0.0101}$.

We found that NGTS-28Ab is orbiting one of the hottest M dwarfs within the transiting BD desert. It is also found to be one of the shortest period transiting BDs within the desert.

ACKNOWLEDGEMENTS

This work is based on data collected under the NGTS project at the European Southern Observatory (ESO) La Silla Paranal Observatory. The NGTS facility is operated by the consortium institutes with support from the UK Science and Technology Facilities Council (STFC) under projects ST/M001962/1, ST/S002642/1, and ST/W003163/1. This study is based on observations collected at the European Southern Observatory under ESO programme 105.20G9. This paper includes public data collected by the TESS mission. Funding for the TESS mission is provided by the NASA Explorer Program. This paper uses observations made at the South African Astronomical Observatory (SAAO). This work has made use of data from the European Space Agency (ESA) mission *Gaia* (https://www.cosmos.esa.int/gaia), processed by the *Gaia* Data Processing and Analysis Consortium (DPAC; https://www.cosmos.esa.int/web/gaia/dpac/consortium). Funding for the DPAC has been provided by national institutions, in particular, the institutions participating in the *Gaia* Multilateral Agreement.

This publication makes use of data products from the Two Micron All Sky Survey, which is a joint project of the University of Massachusetts and the Infrared Processing and Analysis Center/California Institute of Technology, funded by the National Aeronautics and Space Administration and the National Science Foundation. The Pan-STARRS1 Surveys (PS1) and the PS1 public science archive have been made possible through contributions by the Institute for Astronomy, the University of Hawaii, the Pan-STARRS Project Office, the Max-Planck Society and its participating institutes, the Max Planck Institute for Astronomy, Heidelberg and the Max Planck Institute for Extraterrestrial Physics, Garching, The Johns Hopkins University, Durham University, the University of Edinburgh, the Queen's University Belfast, the Harvard-Smithsonian Center for Astrophysics, the Las Cumbres Observatory Global Telescope Network Incorporated, the National Central University of Taiwan, the Space Telescope Science Institute, the National Aeronautics and Space Administration under grant no. NNX08AR22G issued through the Planetary Science Division of the NASA Science Mission Directorate, the National Science Foundation grant no. AST-1238877, the University of Maryland, Eotvos Lorand University (ELTE), the Los Alamos National Laboratory, and the Gordon and Betty Moore Foundation.

Some of the Observations in the paper made use of the high-resolution Imaging instrument Zorro. Zorro was funded by the NASA Exoplanet Exploration Program and built at the NASA Ames Research Center by Steve B. Howell, Nic Scott, Elliott P. Horch, and Emmett Quigley. Zorro was mounted on the Gemini South telescope of the international Gemini Observatory, a programme of NSF's NOIRLab, which is managed by the Association of Universities for Research in Astronomy (AURA) under a cooperative agreement with the National Science Foundation on behalf of the Gemini partnership: the National Science Foundation (United States), National Research Council (Canada), Agencia Nacional de Investigación y Desarrollo (Chile), Ministerio de Ciencia, Tecnología e Innovación (Argentina), Ministério da Ciência, Tecnologia, Inovações e Comunicações (Brazil), and Korea Astronomy and Space Science Institute (Republic of Korea).

BH is supported by an STFC studentship (ST/S505511/1 and ST/T506242/1). SLC acknowledges support from an STFC Ernest Rutherford Fellowship (ST/R003726/1). The contribution of FB, ML, OT, and SU has been carried out within the framework of the NCCR PlanetS supported by the Swiss National Science Foundation under grants 51NF40_182901 and 51NF40_205606. ML acknowledges support of the Swiss National Science Foundation under grant number PCEFP2_194576. The contribution of EMB has been supported by STFC through the consolidated grant ST/W001136/1. CAC acknowledges that this research was carried out at the Jet Propulsion Laboratory, California Institute of Technology, under a contract with NASA (80NM0018D0004). JSJ gratefully acknowledges support by FONDECYT grant 1201371 and from the ANID BASAL projects ACE210002 and FB210003. The postdoctoral fellowship of KB is funded by FRS-FNRS grant T.0109.20 and by the Francqui Foundation. This publication benefits from the support of the French Community of Belgium in the context of the FRIA Doctoral grant awarded to MT. MG is FRS-FNRS Research Director and EJ is FRS–FNRS Senior Research Associate. FJP acknowledges financial support from the grant CEX2021-001131-S funded by MCIN/AEI/10.13039/501100011033 and through projects PID2019-109522GB-C52 and PID2022-137241NB-C43. This research is in part funded by the European Union's Horizon 2020 research and innovation programme (grant agreement no. 803193/BEBOP), from the MERAC foundation, and from the Science and Technology Facilities Council (STFC; grant no. ST/S00193X/1 and ST/W000385/1). Based on data collected by the SPECULOOS-South Observatory at the ESO Paranal Observatory in Chile. The ULiege's contribution to SPECULOOS has received funding from the European Research Councilunder the European Union's Seventh Framework Programme (FP/2007-2013) (grant agreement no. 336480/SPECULOOS), from the Balzan Prize and Francqui Foundations, from the Belgian Scientific Research Foundation (FRS-FNRS; grant no. T.0109.20), from the University of Liege, and from the ARC grant for Concerted Research Actions financed by the Wallonia-Brussels Federation. This work is supported by a grant from the Simons Foundation (PI Queloz, grant number 327127). Based on data collected by the TRAPPIST-South telescope at the ESO La Silla Observatory. TRAPPIST is funded by the Belgian Fund for Scientific Research (Fond National de la Recherche Scientifique, FNRS) under the grant PDR T.0120.21, with the participation of the Swiss National Science Foundation (SNF).

DATA AVAILABILITY

The *TESS* data is available via the MAST (Mikulski Archive for Space Telescopes) portal at https://mast.stsci.edu/portal/Mashup/Clients/Mast/Portal.html. Data can also be downloaded from TFOP for NGTS-28A (TOI-6110) at https://exofop.ipac.caltech.edu/tess/target.php?id=7439480. Public NGTS and HARPS data are available in the ESO archive at http://archive.eso.org/eso/eso_archive_main.html. SAAO data are available on its public archive at https://ssda.saao.ac.za/. The other data within this article will be shared on reasonable request to the corresponding author.

SPECMATCH-EMP, ARIADNE, and ALLESFITTER are open-source and public software.

REFERENCES

Acton J. S. et al., 2021, MNRAS, 505, 2741
Allard F., Homeier D., Freytag B., 2012, Phil. Trans. R. Soc. London Ser. A, 370, 2765
Alves D. R. et al., 2022, MNRAS
Artigau É. et al., 2021, AJ, 162, 144
Astropy Collaboration, 2013, A&A, 558, A33
Astropy Collaboration, 2018, AJ, 156, 123
Astropy Collaboration, 2022, apj, 935, 167
Baraffe I., Chabrier G., Allard F., Hauschildt P. H., 2002, A&A, 382, 563
Baraffe I., Chabrier G., Barman T. S., Allard F., Hauschildt P. H., 2003, A&A, 402, 701
Baraffe I., Homeier D., Allard F., Chabrier G., 2015, A&A, 577, A42
Baranne A. et al., 1996, A&AS, 119, 373
Barkaoui K. et al., 2023, A&A, 677, A38
Bate M. R., Bonnell I. A., Bromm V., 2002, MNRAS, 332, L65
Bayliss D. et al., 2017, AJ, 153, 15
Beatty T. G. et al., 2007, ApJ, 663, 573
Beatty T. G. et al., 2014, ApJ, 783, 112
Benni P. et al., 2021, MNRAS, 505, 4956
Bonomo A. S. et al., 2015, A&A, 575, A85
Bouchy F. et al., 2011, A&A, 525, A68
Bowler B. P., Blunt S. C., Nielsen E. L., 2020, AJ, 159, 63
Broeg C., Fernández M., Neuhäuser R., 2005, Astron. Nachr., 326, 134
Burgasser A. J., 2008, Physics Today, 61, 70
Burrows A., Liebert J., 1993, Rev. Mod. Phys., 65, 301
Carmichael T. W. et al., 2020, AJ, 160, 53
Carmichael T. W. et al., 2021, AJ, 161, 97
Carmichael T. W. et al., 2022, MNRAS, 514, 4944
Carmichael T. W., Latham D. W., Vanderburg A. M., 2019, AJ, 158, 38
Casewell S. L. et al., 2020a, MNRAS, 497, 3571
Casewell S. L., Debes J., Braker I. P., Cushing M. C., Mace G., Marley M. S., Kirkpatrick J. D., 2020b, MNRAS, 499, 5318
Castelli F., Kurucz R., 2004, Proceedings of the 210th Symposium of the International Astronomical Union held at Uppsala University, Uppsala, Sweden, 17-21 June Edited by N. Piskunov, W.W. Weiss, and D.F. Gray.

Published on behalf of the IAU by the Astronomical Society of the Pacific, p. A20
Chambers K. C. et al., 2016, preprint (arXiv:1612.05560)
Chaturvedi P., Chakraborty A., Anandarao B. G., Roy A., Mahadevan S., 2016, MNRAS, 462, 554
Chaturvedi P., Sharma R., Chakraborty A., Anandarao B. G., Prasad N. J. S. S. V., 2018, AJ, 156, 27
Ciardi D. R., Beichman C. A., Horch E. P., Howell S. B., 2015, ApJ, 805, 16
Gaia Collaboration, 2023, A&A, 674, A1
Coppejans R. et al., 2013, PASP, 125, 976
Csizmadia S. et al., 2015, A&A, 584, A13
Csizmadia S., 2016, The CoRoT Legacy Book: The adventure of the ultra high precision photometry from space, by the CoRot Team. EDP Sciences, p. 143
Dall T. H., Santos N. C., Arentoft T., Bedding T. R., Kjeldsen H., 2006, A&A, 454, 341
David T. J., Hillenbrand L. A., Gillen E., Cody A. M., Howell S. B., Isaacson H. T., Livingston J. H., 2019, ApJ, 872, 161
Deleuil M. et al., 2008, A&A, 491, 889
Delrez L. et al., 2018, Ground-based and Airborne Telescopes VII, vol. 10700. Proceedings of the SPIE, p. 446
Díaz R. F. et al., 2013, A&A, 551, L9
Díaz R. F. et al., 2014, A&A, 572, A109
Dransfield G. et al., 2024, MNRAS, 527, 35
Eaton N., Draper P. W., Allan A., Naylor T., Mukai K., Currie M. J., McCaughrean M., 2014, Astrophysics Source Code Library, record ascl:1405.013
Flewelling H. A. et al., 2020, ApJS, 251, 7
Foreman-Mackey D., Hogg D. W., Lang D., Goodman J., 2013, PASP, 125, 306
Furlan E., Howell S. B., 2017, AJ, 154, 66
Gagné J. et al., 2018, ApJ, 856, 23
Gaia Collaboration, 2016, A&A, 595, A1
Garcia L. J., Timmermans M., Pozuelos F. J., Ducrot E., Gillon M., Delrez L., Wells R. D., Jehin E., 2022, MNRAS, 509, 4817
Gill S. et al., 2020, MNRAS, 495, 2713
Gill S. et al., 2022, MNRAS, 513, 1785
Gillen E., Hillenbrand L. A., David T. J., Aigrain S., Rebull L., Stauffer J., Cody A. M., Queloz D., 2017, ApJ, 849, 11
Gillon M., Jehin E., Magain P., Chantry V., Hutsemékers D., Manfroid J., Queloz D., Udry S., 2011, Eur. Phys. J. Web Conf, 11, 06002
Grether D., Lineweaver C. H., 2006, ApJ, 640, 1051
Grieves N. et al., 2017, MNRAS, 467, 4264
Grieves N. et al., 2021, A&A, 652, A127
Günther M. N. et al., 2018, MNRAS, 478, 4720
Günther M. N., Daylan T., 2019, Astrophysics Source Code Library, record ascl:1903.003
Günther M. N., Daylan T., 2021, ApJS, 254, 13
Hauschildt P. H., Allard F., Baron E., 1999, ApJ, 512, 377
Heller R., Jackson B., Barnes R., Greenberg R., Homeier D., 2010, A&A, 514, A22
Heller R., Leconte J., Barnes R., 2011, A&A, 528, A27
Hodžić V. et al., 2018, MNRAS, 481, 5091
Howell S. B., Everett M. E., Sherry W., Horch E., Ciardi D. R., 2011, AJ, 142, 19
Howell S. B., Furlan E., 2022, Front. Astron. Space Sci., 9
Husser T. O., Wende-von Berg S., Dreizler S., Homeier D., Reiners A., Barman T., Hauschildt P. H., 2013, A&A, 553, A6
Irwin J. et al., 2010, ApJ, 718, 1353
Irwin J. M. et al., 2018, AJ, 156, 140
Jackman J. A. G. et al., 2019, MNRAS, 489, 5146
Jackson B., Greenberg R., Barnes R., 2008, ApJ, 678, 1396
Jeffreys H., 1998, The Theory of Probability. Oxford Classic Texts in the Physical Sciences. OUP, Oxford
Jehin E. et al., 2011, Messenger, 145, 2
Jehin E. et al., 2018, Messenger, 174, 2
Jenkins J. M. et al., 2016, in Chiozzi G., Guzman J. C., eds, Proc. SPIE Conf. Ser. Vol. 9913, Software and Cyberinfrastructure for Astronomy IV. SPIE, Bellingham, p. 99133E
Jenkins J. S. et al., 2015, MNRAS, 453, 1439
Johnson J. A. et al., 2011, ApJ, 730, 79
Kass R. E., Raftery A. E., 1995, J. Am. Stat. Assoc., 90, 773
Kipping D. M., 2013, MNRAS, 435, 2152
Kurucz R., 1993, ATLAS9 Stellar Atmosphere Programs and 2 km/s grid. Kurucz CD-ROM No. 13. Cambridge
Latham D. W., Mazeh T., Stefanik R. P., Mayor M., Burki G., 1989, Nature, 339, 38
Lomb N. R., 1976, Ap&SS, 39, 447
Lucy L. B., Sweeney M. A., 1971, AJ, 76, 544
Mugrauer M., 2023, Astronomische Nachrichten, 344, e20230055
Ma B., Ge J., 2014, MNRAS, 439, 2781
Mardling R. A., Lin D. N. C., 2004, ApJ, 614, 955
Marley M. S. et al., 2021, ApJ, 920, 85
Maxted P. F. L., 2016, A&A, 591, A111
Mayor M. et al., 2003, Messenger, 114, 20
Mireles I. et al., 2020, AJ, 160, 133
Moutou C. et al., 2013, A&A, 558, L6
Nakajima T., Oppenheimer B. R., Kulkarni S. R., Golimowski D. A., Matthews K., Durrance S. T., 1995, Nature, 378, 463
Nefs S. V. et al., 2013, MNRAS, 431, 3240
Nowak G. et al., 2017, AJ, 153, 131
Ofir A., Gandolfi D., Buchhave L., Lacy C. H. S., Hatzes A. P., Fridlund M., 2012, MNRAS, 423, L1
Palle E. et al., 2021, A&A, 650, A55
Parsons S. G. et al., 2018, MNRAS, 481, 1083
Parviainen H. et al., 2020, A&A, 633, A28
Parviainen H., Aigrain S., 2015, MNRAS, 453, 3821
Pecaut M. J., Mamajek E. E., 2013, ApJS, 208, 9
Pepe F., Mayor M., Galland F., Naef D., Queloz D., Santos N. C., Udry S., Burnet M., 2002, A&A, 388, 632
Persson C. M. et al., 2019, A&A, 628, A64
Pont F. et al., 2006, A&A, 447, 1035
Pont F., Bouchy F., Melo C., Santos N. C., Mayor M., Queloz D., Udry S., 2005b, A&A, 438, 1123
Pont F., Melo C. H. F., Bouchy F., Udry S., Queloz D., Mayor M., Santos N. C., 2005a, A&A, 433, L21
Psaridi A. et al., 2022, A&A, 664, A94
Queloz D. et al., 2001, A&A, 379, 279
Raghavan D. et al., 2010, ApJS, 190, 1
Rajpurohit A. S., Reylé C., Allard F., Homeier D., Schultheis M., Bessell M. S., Robin A. C., 2013, A&A, 556, A15
Rebolo R., Zapatero Osorio M. R., Martín E. L., 1995, Nature, 377, 129
Ricker G. R. et al., 2014, J. Astron. Telesc. Instrum. Syst., 1, 1
Santos N. C. et al., 2002, A&A, 392, 215
Scargle J. D., 1982, ApJ, 263, 835
Schaffenroth V. et al., 2021, MNRAS, 501, 3847
Science Software Branch at STScI, 2012, Astrophysics Source Code Library, record ascl:1207.011
Scott N. J. et al., 2021, Front. Astron. Space Sci., 8, 138
Sebastian D. et al., 2021, A&A, 645, A100
Shporer A. et al., 2017, ApJ, 847, L18
Siverd R. J. et al., 2012, ApJ, 761, 123
Skrutskie M. F. et al., 2006, AJ, 131, 1163
Speagle J. S., 2020, MNRAS, 493, 3132
Stassun K. G., Mathieu R. D., Valenti J. A., 2006, Nature, 440, 311
STScI Development Team, 2013, Astrophysics Source Code Library, record ascl:1303.023
Šubjak J. et al., 2020, AJ, 159, 151
Tal-Or L. et al., 2013, A&A, 553, A30
Tamuz O., Mazeh T., Zucker S., 2005, MNRAS, 356, 1466
Thorngren D. P., Fortney J. J., Lopez E. D., Berger T. A., Huber D., 2021, ApJ, 909, L16
Tilbrook R. H. et al., 2021, MNRAS, 504, 6018
Tody D., 1986, in Crawford D. L., ed., Proc. SPIE Conf. Ser. Vol. 627, Instrumentation in Astronomy VI. SPIE, Bellingham, p. 733
Tody D., 1993, in Hanisch R. J., Brissenden R. J. V., Barnes J., eds, ASP Conf. Ser. Vol. 52, Astronomical Data Analysis Software and Systems II. Astron. Soc. Pac., San Francisco, p. 173

Triaud A. H. M. J. et al., 2013, A&A, 549, A18
Triaud A. H. M. J. et al., 2017, A&A, 608, A129
Triaud A. H. M. J. et al., 2020, Nature, 4, 650
Vines J. I., Jenkins J. S., 2022, MNRAS, 513, 2719
von Boetticher A. et al., 2017, A&A, 604, L6
von Boetticher A. et al., 2019, A&A, 625, A150
Wheatley P. J. et al., 2018, MNRAS, 475, 4476
Whitworth A., 2018, Handbook of Exoplanets. Springer International Publishing AG, p. 95
Yee S. W., Petigura E. A., von Braun K., 2017, ApJ, 836, 77
Zahn J. P., Bouchet L., 1989, A&A, 223, 112
Zhou G. et al., 2014, MNRAS, 437, 2831
Zhou G. et al., 2019, AJ, 157, 31

APPENDIX: EXTRA DATA, FIGURES, AND TABLES

A1 Full data tables

A2 Corner plots

A3 BD desert population plots

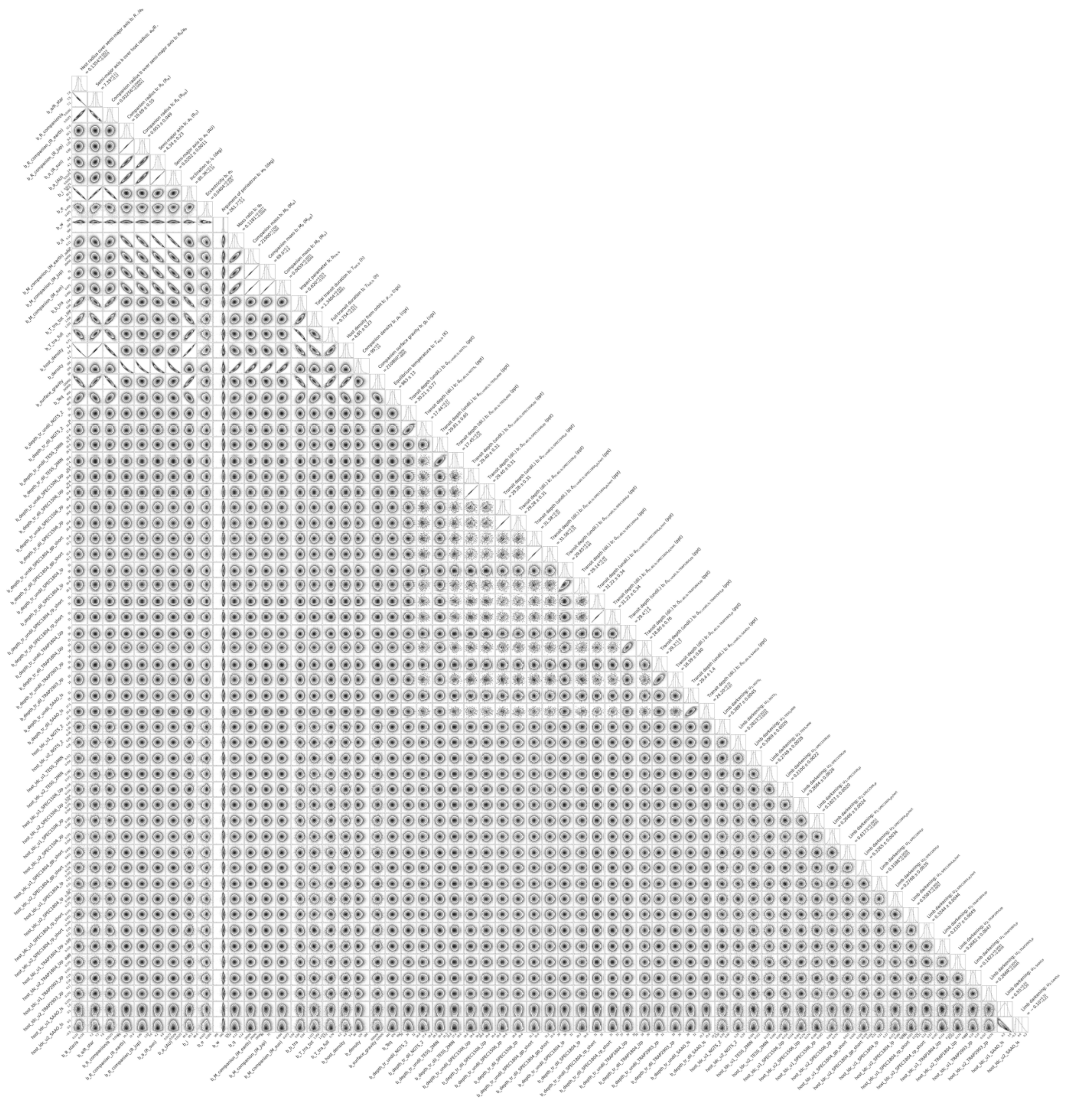

Figure A1. The corner plot for the derived values in the final fit.

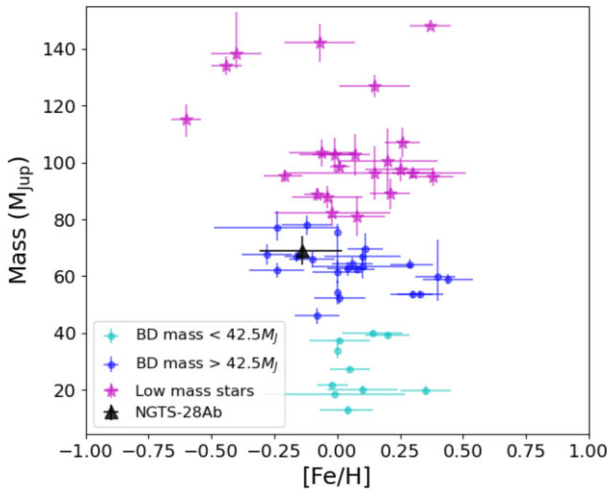

Figure A2. Mass–metallicity plot of objects in Fig. A1. The metallicity is for the host star in each system. NGTS-28Ab is plotted as a black triangle. Low-mass stars are plotted as magenta stars. BDs with masses above 42.5 M_J are dark blue circles and BDs with below 42.5 M_J are light blue circles. RIK-72b (David et al. 2019) and the binary system discovered by Stassun, Mathieu & Valenti (2006) are not included due to their youth.

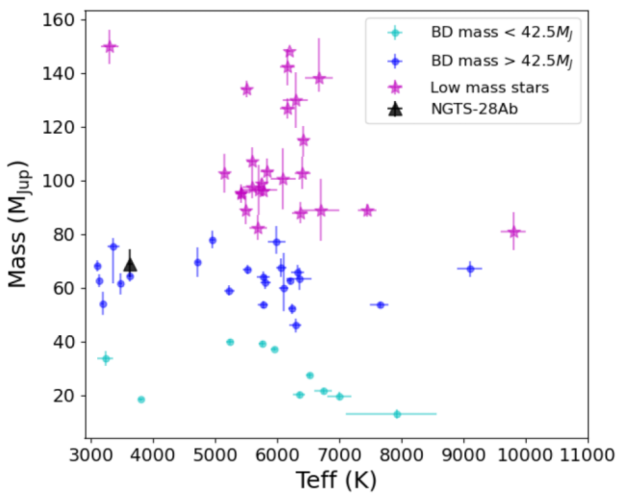

Figure A3. Mass–T_{eff} plot of objects in A1. The T_{eff} values are for the host star in each system. NGTS-28Ab is plotted as a black triangle. Low-mass stars are plotted as magenta stars. BDs with masses above 42.5 M_J are dark blue circles and BDs with below 42.5 M_J are light blue circles. RIK-72b (David et al. 2019) and the binary system discovered by Stassun, Mathieu & Valenti (2006) are not included due to their youth.

Table A1. Parameters of all objects used within the population analysis. RIK-72b (David et al. 2019) and the binary system discovered by Stassun, Mathieu & Valenti (2006) are not included due to their youth and large radii.

Object	P (d)	M_2 (M_J)	R_2 (R_J)	T_{eff} (K)	M_1 ($M_\odot$)	R_1 ($R_\odot$)	ecc	[Fe/H]	Source
HATS-70b	1.89	$12.9^{+1.8}_{-1.6}$	$1.38^{+0.08}_{-0.07}$	7930^{+630}_{-820}	$1.78^{+0.12}_{-0.12}$	$1.88^{+0.06}_{-0.07}$	<0.18	$0.04^{+0.10}_{-0.11}$	(1)
TOI-1278b	14.48	$18.5^{+0.5}_{-0.5}$	$1.09^{+0.24}_{-0.20}$	3799^{+42}_{-42}	$0.55^{+0.02}_{-0.02}$	$0.57^{+0.01}_{-0.01}$	$0.013^{+0.004}_{-0.004}$	$-0.01^{+0.28}_{-0.28}$	(2)
GPX-1b	1.74	$19.7^{+1.6}_{-1.6}$	$1.47^{+0.10}_{-0.10}$	7000^{+200}_{-200}	$1.68^{+0.10}_{-0.10}$	$1.56^{+0.10}_{-0.10}$	0 (fixed)	$0.35^{+0.10}_{-0.10}$	(3)
Kepler-39b	21.09	$20.1^{+1.3}_{-1.2}$	$1.24^{+0.09}_{-0.10}$	6350^{+100}_{-100}	$1.29^{+0.06}_{-0.07}$	$1.40^{+0.10}_{-0.10}$	$0.112^{+0.057}_{-0.057}$	$0.10^{+0.14}_{-0.14}$	(4)
CoRoT-3b	4.26	$21.7^{+1.0}_{-1.0}$	$1.01^{+0.07}_{-0.07}$	6740^{+140}_{-140}	$1.37^{+0.09}_{-0.09}$	$1.56^{+0.09}_{-0.09}$	0 (fixed)	$-0.02^{+0.06}_{-0.06}$	(5)
KELT-1b	1.22	$27.4^{+0.9}_{-0.9}$	$1.12^{+0.04}_{-0.03}$	6516^{+49}_{-49}	$1.34^{+0.06}_{-0.06}$	$1.47^{+0.05}_{-0.04}$	$0.010^{+0.010}_{-0.007}$	$0.05^{+0.08}_{-0.08}$	(6)(7)
NLTT41135b	2.89	$33.7^{+2.8}_{-2.6}$	$1.13^{+0.27}_{-0.17}$	3230^{+130}_{-130}	$0.19^{+0.03}_{-0.02}$	$0.21^{+0.02}_{-0.01}$	<0.02	0 (fixed)	(8)(9)
WASP-128b	2.21	$37.2^{+0.8}_{-0.9}$	$0.94^{+0.02}_{-0.02}$	5950^{+50}_{-50}	$1.16^{+0.04}_{-0.04}$	$1.15^{+0.02}_{-0.02}$	<0.007	$0.01^{+0.12}_{-0.12}$	(10)
CWW89Ab	5.29	$39.2^{+1.1}_{-1.1}$	$0.94^{+0.02}_{-0.02}$	5755^{+49}_{-49}	$1.10^{+0.05}_{-0.05}$	$1.03^{+0.02}_{-0.02}$	$0.189^{+0.002}_{-0.002}$	$0.20^{+0.09}_{-0.09}$	(11)(12)
KOI-205b	11.72	$39.9^{+1.0}_{-1.0}$	$0.81^{+0.02}_{-0.02}$	5237^{+60}_{-60}	$0.93^{+0.03}_{-0.03}$	$0.84^{+0.02}_{-0.02}$	<0.031	$0.14^{+0.12}_{-0.12}$	(13)
TOI-1406b	10.57	$46.0^{+2.6}_{-2.7}$	$0.86^{+0.03}_{-0.03}$	6290^{+100}_{-100}	$1.18^{+0.08}_{-0.09}$	$1.35^{+0.03}_{-0.03}$	$0.026^{+0.013}_{-0.010}$	$-0.08^{+0.09}_{-0.09}$	(14)
EPIC212036875b	5.17	$52.3^{+1.9}_{-1.9}$	$0.87^{+0.02}_{-0.02}$	6238^{+59}_{-60}	$1.29^{+0.07}_{-0.06}$	$1.50^{+0.03}_{-0.03}$	$0.132^{+0.004}_{-0.004}$	$0.01^{+0.10}_{-0.10}$	(12)(15)
TOI-503b	3.68	$53.7^{+1.2}_{-1.2}$	$1.34^{+0.26}_{-0.15}$	7650^{+140}_{-160}	$1.80^{+0.06}_{-0.06}$	$1.70^{+0.05}_{-0.04}$	0 (fixed)	$0.30^{+0.08}_{-0.09}$	(16)
TOI-852b	4.95	$53.7^{+1.4}_{-1.3}$	$0.83^{+0.04}_{-0.04}$	5768^{+84}_{-81}	$1.32^{+0.05}_{-0.04}$	$1.71^{+0.04}_{-0.04}$	$0.004^{+0.004}_{-0.003}$	$0.33^{+0.09}_{-0.09}$	(17)
AD3116b	1.98	$54.2^{+4.3}_{-4.3}$	$1.02^{+0.28}_{-0.28}$	3184^{+29}_{-29}	$0.28^{+0.02}_{-0.02}$	$0.29^{+0.08}_{-0.08}$	$0.146^{+0.024}_{-0.016}$	0 (fixed)	(18)
CoRoT-33b	5.82	$59.0^{+1.8}_{-1.7}$	$1.10^{+0.53}_{-0.53}$	5225^{+80}_{-80}	$0.86^{+0.04}_{-0.04}$	$0.94^{+0.14}_{-0.08}$	$0.070^{+0.002}_{-0.002}$	$0.44^{+0.10}_{-0.10}$	(19)
TOI-811b	25.17	$59.9^{+13.0}_{-8.6}$	$1.26^{+0.06}_{-0.06}$	6107^{+77}_{-77}	$1.32^{+0.05}_{-0.07}$	$1.27^{+0.06}_{-0.09}$	$0.509^{+0.075}_{-0.075}$	$0.40^{+0.07}_{-0.09}$	(17)
TOI-263b	0.56	$61.6^{+4.0}_{-4.0}$	$0.91^{+0.07}_{-0.07}$	3471^{+33}_{-33}	$0.44^{+0.04}_{-0.04}$	$0.44^{+0.03}_{-0.03}$	$0.017^{+0.009}_{-0.010}$	$0.00^{+0.10}_{-0.10}$	(20)(21)
KOI-415b	166.79	$62.1^{+2.7}_{-2.7}$	$0.79^{+0.12}_{-0.07}$	5810^{+80}_{-80}	$0.94^{+0.06}_{-0.06}$	$1.25^{+0.15}_{-0.10}$	$0.698^{+0.002}_{-0.002}$	$-0.24^{+0.11}_{-0.11}$	(22)
WASP-30b	4.16	$62.5^{+1.2}_{-1.2}$	$0.95^{+0.03}_{-0.02}$	6202^{+42}_{-51}	$1.25^{+0.03}_{-0.04}$	$1.39^{+0.03}_{-0.03}$	<0.004	$0.08^{+0.07}_{-0.05}$	(23)
LHS6343c	12.71	$62.7^{+2.4}_{-2.4}$	$0.83^{+0.02}_{-0.02}$	3130^{+20}_{-20}	$0.37^{+0.01}_{-0.01}$	$0.38^{+0.01}_{-0.01}$	$0.056^{+0.032}_{-0.032}$	$0.04^{+0.08}_{-0.08}$	(24)
CoRoT-15b	3.06	$63.3^{+4.1}_{-4.1}$	$1.12^{+0.30}_{-0.15}$	6350^{+200}_{-200}	$1.32^{+0.12}_{-0.12}$	$1.46^{+0.31}_{-0.14}$	0 (fixed)	$0.10^{+0.20}_{-0.20}$	(25)
TOI-569b	6.56	$64.1^{+1.9}_{-1.4}$	$0.75^{+0.02}_{-0.02}$	5768^{+110}_{-92}	$1.21^{+0.05}_{-0.05}$	$1.48^{+0.03}_{-0.03}$	$0.002^{+0.002}_{-0.001}$	$0.29^{+0.09}_{-0.08}$	(14)
TOI-2119b	7.20	$64.4^{+2.3}_{-2.2}$	$1.08^{+0.03}_{-0.03}$	3621^{+48}_{-46}	$0.53^{+0.02}_{-0.02}$	$0.50^{+0.02}_{-0.02}$	$0.337^{+0.002}_{-0.001}$	$0.06^{+0.08}_{-0.08}$	(26)
TOI-1982b	17.17	$65.9^{+2.8}_{-2.7}$	$1.08^{+0.04}_{-0.04}$	6325^{+110}_{-110}	$1.41^{+0.08}_{-0.08}$	$1.51^{+0.05}_{-0.05}$	$0.272^{+0.014}_{-0.014}$	$-0.10^{+0.09}_{-0.09}$	(27)
NGTS-28Ab	1.25	$69.0^{+5.3}_{-4.8}$	0.95 ± 0.05	3626^{+47}_{-44}	$0.56^{+0.02}_{-0.02}$	$0.59^{+0.03}_{-0.03}$	$0.040^{+0.007}_{-0.010}$	$-0.14^{+0.16}_{-0.17}$	This work
EPIC201702477b	40.74	$66.9^{+1.7}_{-1.7}$	$0.76^{+0.07}_{-0.07}$	5517^{+70}_{-70}	$0.87^{+0.03}_{-0.03}$	$0.90^{+0.06}_{-0.06}$	$0.228^{+0.003}_{-0.003}$	$-0.16^{+0.05}_{-0.05}$	(28)
TOI-629b	8.72	$67.0^{+3.0}_{-3.0}$	$1.11^{+0.05}_{-0.05}$	9100^{+200}_{-200}	$2.16^{+0.13}_{-0.13}$	$2.37^{+0.11}_{-0.11}$	$0.298^{+0.008}_{-0.008}$	$0.10^{+0.15}_{-0.15}$	(27)
TOI-2543b	7.54	$67.6^{+3.5}_{-3.5}$	$0.95^{+0.09}_{-0.09}$	6060^{+82}_{-82}	$1.29^{+0.08}_{-0.08}$	$1.86^{+0.15}_{-0.15}$	$0.009^{+0.003}_{-0.002}$	$-0.28^{+0.10}_{-0.10}$	(27)
LP261-75b	1.88	$68.1^{+2.1}_{-2.1}$	$0.90^{+0.01}_{-0.01}$	3100^{+50}_{-50}	$0.30^{+0.02}_{-0.02}$	$0.31^{+0.00}_{-0.00}$	<0.007	–	(29)
NGTS-19b	17.84	$69.5^{+5.7}_{-5.4}$	$1.03^{+0.06}_{-0.05}$	4716^{+39}_{-28}	$0.81^{+0.04}_{-0.04}$	$0.90^{+0.04}_{-0.04}$	$0.377^{+0.006}_{-0.006}$	$0.11^{+0.07}_{-0.07}$	(30)
NGTS-7Ab	0.68	$75.5^{+3.0}_{-13.7}$	$1.38^{+0.13}_{-0.14}$	3359^{+106}_{-89}	$0.48^{+0.03}_{-0.12}$	$0.61^{+0.06}_{-0.06}$	0 (fixed)	0 (fixed)	(31)
TOI-148b	4.87	$77.1^{+5.8}_{-4.6}$	$0.81^{+0.05}_{-0.06}$	5990^{+140}_{-140}	$0.97^{+0.12}_{-0.09}$	$1.20^{+0.07}_{-0.07}$	$0.005^{+0.006}_{-0.004}$	$-0.24^{+0.25}_{-0.25}$	(32)
KOI-189b	30.36	$78.0^{+3.4}_{-3.4}$	$1.00^{+0.02}_{-0.02}$	4952^{+40}_{-40}	$0.76^{+0.05}_{-0.05}$	$0.73^{+0.02}_{-0.02}$	$0.275^{+0.004}_{-0.004}$	$-0.12^{+0.10}_{-0.10}$	(33)
TOI-587b	8.04	$81.1^{+7.1}_{-7.0}$	$1.32^{+0.07}_{-0.06}$	9800^{+200}_{-200}	$2.33^{+0.12}_{-0.12}$	$2.01^{+0.09}_{-0.09}$	$0.051^{+0.049}_{-0.036}$	$0.08^{+0.11}_{-0.12}$	(32)
TOI-746b	10.98	$82.2^{+4.9}_{-4.4}$	$0.95^{+0.09}_{-0.06}$	5690^{+140}_{-140}	$0.94^{+0.09}_{-0.08}$	$0.97^{+0.04}_{-0.03}$	$0.199^{+0.003}_{-0.003}$	$-0.02^{+0.23}_{-0.23}$	(32)
EBLM-J0555 − 57Ab	7.76	$87.9^{+4.0}_{-4.0}$	$0.82^{+0.13}_{-0.06}$	6368^{+124}_{-124}	$1.18^{+0.08}_{-0.08}$	$1.00^{+0.14}_{-0.07}$	$0.090^{+0.004}_{-0.004}$	$-0.04^{+0.14}_{-0.14}$	(34)(35)
TOI-681b	15.78	$88.7^{+2.5}_{-2.3}$	$1.52^{+0.25}_{-0.15}$	7440^{+150}_{-140}	$1.54^{+0.06}_{-0.05}$	$1.47^{+0.04}_{-0.04}$	$0.093^{+0.022}_{-0.019}$	$-0.08^{+0.05}_{-0.05}$	(32)
OGLE-TR−123b	1.80	$89.0^{+11.5}_{-11.5}$	$1.29^{+0.09}_{-0.09}$	6700^{+300}_{-300}	$1.29^{+0.26}_{-0.26}$	$1.55^{+0.10}_{-0.10}$	0 (fixed)	–	(36)
TOI-694b	48.05	$89.0^{+5.3}_{-5.3}$	$1.11^{+0.02}_{-0.02}$	5496^{+87}_{-81}	$0.97^{+0.05}_{-0.04}$	$1.00^{+0.01}_{-0.01}$	$0.519^{+0.001}_{-0.001}$	$0.21^{+0.08}_{-0.08}$	(37)
KOI-607b	5.89	$95.1^{+3.3}_{-3.4}$	$1.09^{+0.09}_{-0.06}$	5418^{+87}_{-85}	$0.99^{+0.05}_{-0.05}$	$0.92^{+0.03}_{-0.03}$	$0.395^{+0.009}_{-0.009}$	$0.38^{+0.08}_{-0.09}$	(12)
J1219-39b	6.76	$95.4^{+1.9}_{-2.5}$	$1.14^{+0.07}_{-0.05}$	5412^{+81}_{-65}	$0.83^{+0.03}_{-0.03}$	$0.81^{+0.04}_{-0.02}$	$0.055^{+0.000}_{-0.000}$	$-0.21^{+0.07}_{-0.08}$	(23)
TIC-320687387 B	29.77	$96.2^{+1.9}_{-2.0}$	$1.14^{+0.02}_{-0.02}$	5780^{+80}_{-80}	$1.08^{+0.03}_{-0.03}$	$1.16^{+0.02}_{-0.02}$	$0.366^{+0.003}_{-0.003}$	$0.30^{+0.08}_{-0.08}$	(38)
OGLE-TR−122b	7.27	$96.4^{+9.4}_{-9.4}$	$1.17^{+0.23}_{-0.13}$	5700^{+300}_{-300}	$0.98^{+0.14}_{-0.14}$	$1.05^{+0.20}_{-0.09}$	$0.205^{+0.008}_{-0.008}$	$0.15^{+0.36}_{-0.36}$	(39)
TOI-1213b	27.22	$97.5^{+4.4}_{-4.2}$	$1.66^{+0.78}_{-0.55}$	5590^{+150}_{-150}	$0.99^{+0.07}_{-0.06}$	$0.99^{+0.04}_{-0.04}$	$0.498^{+0.003}_{-0.002}$	$0.25^{+0.13}_{-0.14}$	(32)
K2-76b	11.99	$98.7^{+2.0}_{-2.0}$	$0.89^{+0.05}_{-0.03}$	5747^{+70}_{-64}	$0.96^{+0.03}_{-0.03}$	$1.17^{+0.06}_{-0.03}$	$0.255^{+0.007}_{-0.007}$	$0.01^{+0.04}_{-0.04}$	(40)
CoRoT-101186644	20.68	$100.6^{+11.5}_{-11.5}$	$1.01^{+0.25}_{-0.06}$	6090^{+200}_{-200}	$1.20^{+0.20}_{-0.20}$	$1.07^{+0.07}_{-0.07}$	$0.402^{+0.006}_{-0.006}$	$0.20^{+0.20}_{-0.20}$	(41)
J2343+29Ab	16.95	$102.7^{+7.3}_{-7.3}$	$1.24^{+0.07}_{-0.07}$	5150^{+90}_{-60}	$0.86^{+0.10}_{-0.10}$	$0.85^{+0.05}_{-0.06}$	$0.161^{+0.002}_{-0.003}$	$0.07^{+0.01}_{-0.17}$	(42)
EBLM-J0954 − 23Ab	7.57	$102.8^{+5.9}_{-6.0}$	$0.98^{+0.17}_{-0.17}$	6406^{+124}_{-124}	$1.17^{+0.08}_{-0.08}$	$1.23^{+0.17}_{-0.17}$	$0.042^{+0.001}_{-0.001}$	$-0.01^{+0.14}_{-0.14}$	(35)

Table A1 – *continued*

Object	P (d)	M_2 (M_J)	R_2 (R_J)	T_{eff} (K)	M_1 ($M_\odot$)	R_1 ($R_\odot$)	ecc	[Fe/H]	Source
KOI-686b	52.51	$103.4^{+4.8}_{-4.8}$	$1.22^{+0.04}_{-0.04}$	5834^{+100}_{-100}	$0.98^{+0.07}_{-0.07}$	$1.04^{+0.03}_{-0.03}$	$0.556^{+0.004}_{-0.004}$	$-0.06^{+0.13}_{-0.13}$	(33)
TIC-220568520b	18.56	$107.2^{+5.2}_{-5.2}$	$1.25^{+0.02}_{-0.02}$	5589^{+81}_{-81}	$1.03^{+0.04}_{-0.04}$	$1.01^{+0.01}_{-0.01}$	$0.096^{+0.003}_{-0.003}$	$0.26^{+0.07}_{-0.07}$	(37)
HATS550-016B	2.05	$115.2^{+5.2}_{-6.3}$	$1.43^{+0.03}_{-0.04}$	6420^{+90}_{-90}	$0.97^{+0.05}_{-0.06}$	$1.22^{+0.02}_{-0.03}$	$0.080^{+0.020}_{-0.020}$	$-0.60^{+0.06}_{-0.06}$	(43)
OGLE-TR−106b	2.54	$121.5^{+22.0}_{-22.0}$	$1.76^{+0.13}_{-0.13}$	–	–	$1.31^{+0.09}_{-0.09}$	$0.000^{+0.020}_{-0.020}$	–	(44)
EBLM-J1431 − 11Ab	4.45	$126.9^{+3.8}_{-3.9}$	$1.45^{+0.07}_{-0.05}$	6161^{+124}_{-124}	$1.20^{+0.06}_{-0.06}$	$1.11^{+0.04}_{-0.03}$	0 (fixed)	$0.15^{+0.14}_{-0.14}$	(35)
HAT-TR-205-013B	2.23	$129.9^{+10.5}_{-10.5}$	$1.63^{+0.06}_{-0.06}$	6295^{+200}_{-200}	$1.04^{+0.13}_{-0.13}$	$1.28^{+0.04}_{-0.04}$	$0.012^{+0.021}_{-0.021}$	–	(45)
TIC-231005575b	61.78	$134.1^{+3.1}_{-3.1}$	$1.50^{+0.08}_{-0.08}$	5500^{+85}_{-85}	$1.05^{+0.04}_{-0.04}$	$0.99^{+0.05}_{-0.05}$	$0.298^{+0.001}_{-0.004}$	$-0.44^{+0.06}_{-0.06}$	(46)
HATS551-021B	3.64	$138.3^{+14.7}_{-5.2}$	$1.50^{+0.06}_{-0.08}$	6670^{+220}_{-220}	$1.10^{+0.10}_{-0.10}$	$1.20^{+0.08}_{-0.01}$	$0.060^{+0.020}_{-0.020}$	$-0.40^{+0.10}_{-0.10}$	(43)
EBLM-J2017+02Ab	0.82	$142.2^{+6.6}_{-6.7}$	$1.49^{+0.13}_{-0.10}$	6161^{+124}_{-124}	$1.11^{+0.07}_{-0.07}$	$1.20^{+0.08}_{-0.05}$	0 (fixed)	$-0.07^{+0.14}_{-0.14}$	(35)
KIC-1571511B	14.02	$148.1^{+0.5}_{-0.4}$	$1.74^{+0.00}_{-0.01}$	6195^{+50}_{-50}	$1.27^{+0.04}_{-0.03}$	$1.34^{+0.01}_{-0.01}$	$0.327^{+0.003}_{-0.003}$	$0.37^{+0.08}_{-0.08}$	(47)
WTS-19G-4-02069B	2.44	$149.8^{+6.3}_{-6.3}$	$1.69^{+0.06}_{-0.06}$	3300^{+140}_{-140}	$0.53^{+0.02}_{-0.02}$	$0.51^{+0.01}_{-0.01}$	0 (fixed)	–	(48)

Note. The table has been adapted and updated from Grieves et al. (2021).

Sources: (1): Zhou et al. (2019), (2): Artigau et al. (2021), (3): Benni et al. (2021), (4): Bonomo et al. (2015), (5): Deleuil et al. (2008), (6): Siverd et al. (2012), (7): Beatty et al. (2014), (8): Irwin et al. (2010), (9): Csizmadia (2016), (10): Hodžić et al. (2018), (11): Nowak et al. (2017), (12): Carmichael, Latham & Vanderburg (2019), (13): Díaz et al. (2013), (14): Carmichael et al. (2020), (15): Persson et al. (2019), (16): Šubjak et al. (2020), (17): Carmichael et al. (2021), (18): Gillen et al. (2017), (19): Csizmadia et al. (2015), (20): Parviainen et al. (2020), (21): Palle et al. (2021), (22): Moutou et al. (2013), (23): Triaud et al. (2013), (24): Johnson et al. (2011), (25): Bouchy et al. (2011), (26): Carmichael et al. (2022), (27): Psaridi et al. (2022), (28): Bayliss et al. (2017), (29): Irwin et al. (2018), (30): Acton et al. (2021), (31): Jackman et al. (2019), (32): Grieves et al. (2021), (33): Díaz et al. (2014), (34): von Boetticher et al. (2017), (35): von Boetticher et al. (2019), (36): Pont et al. (2006), (37): Mireles et al. (2020), (38): Gill et al. (2022),(39):Pont et al. (2005a), (40): Shporer et al. (2017), (41): Tal-Or et al. (2013), (42): Chaturvedi et al. (2016), (43): Zhou et al. (2014), (44): Pont et al. (2005b), (45): Beatty et al. (2007), (46): Gill et al. (2020), (47): Ofir et al. (2012), (48): Nefs et al. (2013).

[1]*School of Physics and Astronomy, University of Leicester, University Road, Leicester LE1 7RH, UK*
[2]*European Space Agency (ESA), European Space Research and Technology Centre (ESTEC), Keplerlaan 1, NL-2201 AZ Noordwijk, the Netherlands*
[3]*European Southern Observatory, Karl-Schwarzschildstr. 2, D-85748 Garching bei München, Germany*
[4]*Département d'astronomie, Université de Genéve, 51 chemin Pegasi, CH-1290 Sauverny, Switzerland*
[5]*NASA Ames Research Center, Moffett Field, CA 94035, USA*
[6]*Jet Propulsion Laboratory, California Institute of Technology, Pasadena, CA 91109, USA*
[7]*NASA Exoplanet Science Institute, IPAC, California Institute of Technology, Pasadena, CA 91125, USA*
[8]*Bay Area Environmental Research Institute, Moffett Field, CA 94035, USA*
[9]*Astrobiology Research Unit, Université de Liège, Allée du 6 Août 19C, B-4000 Liège, Belgium*
[10]*Department of Earth, Atmospheric and Planetary Science, Massachusetts Institute of Technology, 77 Massachusetts Avenue, Cambridge, MA 02139, USA*
[11]*Instituto de Astrofísica de Canarias (IAC), Calle Vía Láctea s/n, 38200, La Laguna, Tenerife, Spain*
[12]*Departamento de Astronomía, Universidad de Chile, Casilla 36-D, Santiago, Chile*
[13]*Centro de Astrofísica y Tecnologías Afines (CATA), Casilla 36-D, Santiago, Chile*
[14]*Centre for Exoplanets and Habitability, University of Warwick, Gibbet Hill Road, Coventry CV4 7AL, UK*
[15]*Department of Physics, University of Warwick, Gibbet Hill Road, Coventry CV4 7AL, UK*
[16]*Mullard Space Science Laboratory, University College London, Holmbury St Mary, Dorking, Surrey RH5 6NT, UK*
[17]*School of Physics & Astronomy, University of Birmingham, Edgbaston, Birmingham B15 2TT, UK*
[18]*AIM, CEA, CNRS, Université Paris-Saclay, Université de Paris, F-91191 Gif-sur-Yvette, France*
[19]*Institute of Planetary Research, German Aerospace Center, Rutherfordstrasse 2, D-12489 Berlin, Germany*
[20]*Astronomy Unit, Queen Mary University of London, Mile End Road, London E1 4NS, UK*
[21]*Astrophysics Group, Cavendish Laboratory, J.J. Thomson Avenue, Cambridge CB3 0HE, UK*
[22]*Cavendish Laboratory, JJ Thomson Avenue, Cambridge CB3 0HE, UK*
[23]*School of Earth and Space Exploration, Arizona State University, Tempe, AZ 85287, USA*
[24]*STAR Institute, University of Liége, Allée du 6 Août 19c, B-4000 Liége, Belgium*
[25]*Núcleo de Astronomía, Facultad de Ingeniería y Ciencias, Universidad Diego Portales, Av. Ejército 441, Santiago, Chile*
[26]*Instituto de Astronomía, Universidad Católica del Norte, Angamos 0610, Antofagasta 1270709, Chile*
[27]*Department of Physics, ETH Zurich, Wolfgang-Pauli-Strasse 2, CH-8093 Zurich, Switzerland*
[28]*Instituto de Astrofísica de Andalucía (IAA-CSIC), Glorieta de la Astronomía s/n, E-18008 Granada, Spain*
[29]*Armagh Observatory & Planetarium, College Hill, Armagh BT61 9DG, UK*
[30]*South African Astronomical Observatory, PO Box 9, Observatory 7935, Cape Town, South Africa*
[31]*Astrophysics Research Centre, School of Mathematics and Physics, Queen's University Belfast, BT7 1NN Belfast, UK*

This paper has been typeset from a TEX/LATEX file prepared by the author.